Size Effects During Nanoindentation: Molecular Dynamics Simulation

2

George Z. Voyiadjis and Mohammadreza Yaghoobi

Contents

Abstract

In this chapter, the molecular dynamics (MD) simulation of nanoindentation experiment is revisited. The MD simulation provides valuable insight into the atomistic process occurring during nanoindentation. First, the simulation details and methodology for MD analysis of nanoindentation are presented. The effects of boundary conditions on the nanoindentation response are studied in more detail. The dislocation evolution patterns are then studied using the information provided by atomistic simulation. Different characteristics of metallic sample during nanoindentation experiment, which have been predicted by theoretical models, are investigated. Next, the nature of size effects in samples with small length scales are studied during nanoindentation. The results indicate that the size effects at small indentation depths cannot be modeled using the forest

G. Z. Voyiadjis (✉) · M. Yaghoobi
Department of Civil and Environmental Engineering, Louisiana State University, Baton Rouge, LA, USA
e-mail: voyiadjis@eng.lsu.edu; myagho1@lsu.edu

G. Z. Voyiadjis (ed.), *Handbook of Nonlocal Continuum Mechanics for Materials and Structures*, https://doi.org/10.1007/978-3-319-58729-5_41

hardening model, and the source exhaustion mechanism controls the size effects at the initial stages of nanoindentation. The total dislocation length increases by increasing the dislocation density which reduces the material strength according to the exhaustion hardening mechanisms. The dislocation interactions with each other become important as the dislocation content increases. Finally, the effects of grain boundary (GB) on the controlling mechanisms of size effects are studied using molecular dynamics.

Keywords
Nanoindentation · Molecular dynamics · Size effects · Dislocation · Grain boundary

Introduction

Indentation is a common experiment to investigate the material properties at different length scales. During indentation, a required force to press a hard indenter into the sample is measured. In the case of nanoindentation, unlike the traditional indentation experiment, it has been observed that the hardness is not a constant value and varies during the test (Nix and Gao 1998; Al-Rub and Voyiadjis 2004; Voyiadjis and Al-Rub 2005). Many researchers have tried to study the variation of hardness, which is commonly termed as size effects, during nanoindentation. The variation of geometrically necessary dislocations (GNDs) density has been commonly considered as the mechanism which controls the hardness. Corcoran et al. (1997) investigated the dislocation nucleation and its effects on the response of Au during nanoindentation experiment. Suresh et al. (1999) studied the effects of sample thickness on the mechanical and dislocation nucleation of Cu thin films during nanoindentation. The grain boundary (GB) effects on the defect nucleation and evolution of bicrystal Fe-14 wt. %Si alloy during nanoindentation were investigated by Soer and De Hosson (2005). It was observed that the dislocations pile up against the GB (Soer and De Hosson 2005). Almasri and Voyiadjis (2010) conducted the nanoindentation of polycrystalline thin films and observed that the GB may enhance the sample hardness.

The interaction of dislocations with each other governs the material strength in bulk metallic samples which are usually captured by Taylor-like hardening models (Nix and Gao 1998; Al-Rub and Voyiadjis 2004; Voyiadjis and Al-Rub 2005). The models generally relate the strength to the dislocation density and state that the stress increases by increasing the dislocation density. Recently, researchers have been able to experimentally measure the GNDs content in samples of confined volume (Kysar and Briant 2002; Kysar et al. 2007; Zaafarani et al. 2008; Demir et al. 2009; Dahlberg et al. 2014). However, the experimental observations cannot be fully described by the bulk size models. Demir et al. (2009, 2010) conducted the nanoindentation and microbending experiments and observed that the governing mechanisms of size effects at smaller length scales

are not similar to those of the large size samples. Demir et al. (2009) observed that the hardness decreases by increasing the GNDs density during nanoindentation of Cu single crystal thin films which cannot be described using the bulk-sized models. Demir et al. (2010) also showed the breakage of the dislocations mean-field theory at small length scales during the microbending of Cu single crystal thin films.

One approach to investigate the governing atomistic process of size effects during nanoindentation is to simulate the sample with the full atomistic details using MD. Many deformation mechanisms during nanoindentation of metallic thin films have been captured using MD. Incorporating the MD simulation, Kelchner et al. (1998) investigated the defect nucleation and evolution of Au during nanoindentation. The surface step effects on the response of Au during nanoindentation were investigated by Zimmerman et al. (2001) using atomistic simulation. Lee et al. (2005) conducted a comprehensive study on the defect nucleation and evolution patterns during nanoindentation of Al and tried to explain the nanoindentation response using those patterns. Hasnaoui et al. (2004), Jang and Farkas (2007), and Kulkarni et al. (2009) have studied the interaction between the dislocations and GB during nanoindentation experiment using molecular dynamics. Yaghoobi and Voyiadjis (2014) investigated the effects of the MD boundary conditions on the sample response and defect nucleation and evolution patterns during nanoindentation. Voyiadjis and Yaghoobi (2015) investigated the theoretical models developed to capture the size effects during nanoindentation using MD. Yaghoobi and Voyiadjis (2016a) investigated the governing mechanisms of size effects during nanoindentation using MD. Voyiadjis and Yaghoobi (2016) incorporated large-scale MD to study the GB effects on the material strength as the grain size varies.

This chapter is designed as follows. In section "Simulation Methodology," the general details for atomistic simulation of nanoindentation are described. In section "Boundary Conditions Effects," the effects of selected boundary conditions for MD simulation of nanoindentation are elaborated. In section "Comparing MD Results with Theoretical Models," the obtained results from MD simulation are compared to those predicted by the available theoretical models. In section "Size Effects in Small-Length Scales During Nanoindentation," the governing mechanisms of size effects in thin films of confined volumes are presented. In section "Effects of Grain Boundary on the Nanoindentation Response of Thin Films," the effects of grain boundary and grain size on the nanoindentation response of thin films are elaborated using the results obtained from MD simulation.

Simulation Methodology

The Newton's equations of motion for N interacting monoatomic molecules can be described as below:

$$m_i \ddot{\mathbf{r}}_i = -\nabla_i U + \mathbf{f}_i, i = 1, 2, \ldots, N \tag{1}$$

where $\ddot{\mathbf{r}}_i$ is the second time derivative of i^{th} particle trajectory $\mathbf{r}_i$, m_i is the mass of i^{th} particle, $\mathbf{f}_i$ is an external force on the i^{th} particle, and

$$\nabla_i U = \left(\frac{\partial}{\partial x_i} + \frac{\partial}{\partial y_i} + \frac{\partial}{\partial z_i} \right) U, i = 1, 2, \ldots, N \tag{2}$$

where $U(\mathbf{r}_1, \mathbf{r}_2, \ldots, \mathbf{r}_N)$ is the potential energy. A metallic system can be described using Eq. 1 by approximating the atoms as mass points. Equation 1 should be numerically solved for the whole system. In the case of atomistic simulation, N can be a large number, and a very efficient parallel code should be used to solve the equation. The atomic interactions in metallic systems have been modeled using many different potentials such as Lennard–Jones (LJ), Morse, embedded-atom method (EAM), and modified embedded-atom method (MEAM).

The LJ potential E^{LJ} can be described as below:

$$E^{\mathrm{LJ}}\left(r_{\mathrm{ij}}\right) = 4\varepsilon \left[\left(\frac{\sigma}{r_{\mathrm{ij}}} \right)^{12} - \left(\frac{\sigma}{r_{\mathrm{ij}}} \right)^{6} \right] \tag{3}$$

where σ is the distance from the atom at which $E^{\mathrm{LJ}} = 0$ and ε is the potential well depth. A cutoff distance should be chosen for LJ potential.

Morse potential E^{Morse} can be written as follows:

$$E^{\mathrm{Morse}}\left(r_{\mathrm{ij}}\right) = D \left\{ e^{\left[-2\alpha\left(r_{\mathrm{ij}} - r_0\right)\right]} - 2e^{\left[-\alpha\left(r_{\mathrm{ij}} - r_0\right)\right]} \right\} \tag{4}$$

where D is the cohesive energy, α is the elastic parameter, and r_0 is the equilibrium distance.

EAM is a popular potential to model the metallic atoms interactions (Daw and Baskes 1984). The EAM potential E^{EAM} is described as below:

$$E^{\mathrm{EAM}}\left(r_{\mathrm{ij}}\right) = \frac{1}{2} \sum_{i,j} V\left(r_{\mathrm{ij}}\right) + \sum_{i} F\left(\rho_i\right), \quad \rho_i = \sum_{i \neq j} \varphi\left(r_{\mathrm{ij}}\right) \tag{5}$$

where $V(r_{\mathrm{ij}})$ is the pair interaction potential, $F(\rho_i)$ denotes the embedding potentials, and $\varphi(r_{\mathrm{ij}})$ is a function which is defined using the electron charge density.

The MEAM potential is the modification of EAM potential which can be described as follows (Baskes 1992):

$$E^{\mathrm{MEAM}}\left(r_{\mathrm{ij}}\right) = \frac{1}{2} \sum_{i,j} V\left(r_{\mathrm{ij}}\right) + \sum_{i} F\left(\rho_i'\right) \tag{6}$$

where

$$\rho_i' = \sum_{i \neq j} \varphi\left(r_{\mathrm{ij}}\right) + \frac{1}{2} \sum_{k,j \neq i} f_{\mathrm{ij}}\left(r_{\mathrm{ij}}\right) f_{\mathrm{ik}}\left(r_{\mathrm{ik}}\right) g_i\left(\cos\theta_{\mathrm{ijk}}\right) \tag{7}$$

θ_{ijk} is the angle between the i^{th}, j^{th}, and k^{th} atoms. The explicit three-body term is included by introducing the functions f_{ij}, f_{ik}, and g_i.

The indenter can be modeled as a cluster of atoms. However, in order to manage the computational costs, the indenter is commonly modeled as a repulsive potential. Two types of repulsive models can be used to simulate the interaction between the indenter and thin film atoms:

- First, the spherical indenter is modeled using an indenter repulsive force which is described as below (Yaghoobi and Voyiadjis 2014):

$$\begin{aligned} F^{ind}(r) &= -K^{ind}(r-R)^2 \quad \text{for} \quad r < R \\ F^{ind}(r) &= 0 \qquad\qquad\qquad\quad \text{for} \quad r \geq R \end{aligned} \tag{8}$$

  where K^{ind} is the force constant, r is the atomic distance to the indenter surface, and R is the radius of indenter.
- Second, the indenter, with general geometry can be simplified using a repulsive potential which is described as below (Voyiadjis and Yaghoobi 2015):

$$E^{ind}(r) = \varepsilon^{ind}(r - r_c)^2 r < r_c \tag{9}$$

  where ε^{ind} is the force constant, r is the distance between the particle and indenter surface, and r_c is the cutoff distance.

Five different indenter geometries of right square prismatic, spherical, cylindrical, blunt conical, and conical with the spherical tip are incorporated in this chapter. During nanoindentation, the precise contact area (A) should be captured to calculate the hardness at each step. A 2D-mesh is produced from the projections of atoms in contact with the indenter. The total contact area is then calculated using the obtained 2-D mesh.

The true indentation depth h is different from the tip displacement d during nanoindentation. A conical indenter of h can be obtained as below:

$$h = \frac{(a_c - a_0)}{\tan\theta} \tag{10}$$

where θ is the cone semi-angle, $a_c = \sqrt{A/\pi}$ is the contact radius, and $a_0 = r_2 + r_c(1/\cos\theta - \tan\theta)$. The indentation depth of a spherical indenter is obtained as below:

$$h = R - \sqrt{R^2 - a_c^2} \tag{11}$$

In the case of a conical indenter with the spherical tip, h can be calculated using Eq. 11 for the spherical part. The indentation depth can be obtained as follows for the conical part:

$$h = \frac{(a_c - a_0)}{\tan(\theta/2)} + h_0 \tag{12}$$

where h_0 is the depth at which the indenter geometry changes from spherical to conical, and a_0 is the contact radius at h_0 (Fig. 1). In the cases of cylindrical and right square prismatic indenters, it is assumed that $h \approx d$ because there is no relation between indentation depth and contact area.

In order to visualize the defects, several methods have been introduced such as energy filtering, bond order, centrosymmetry parameter, adaptive common neighbor analysis, Voronoi analysis, and neighbor distance analysis which have been compared with each other by Stukowski (2012). Also, the Crystal Analysis Tool developed by Stukowski and his coworkers (Stukowski and Albe 2010; Stukowski et al. 2012; Stukowski 2012, 2014) have been incorporated to extract the dislocations from the atomistic data. Here, centrosymmetry parameter (*CSP*) and Crystal Analysis Tool are explained in more detail. *CSP* can be described as below (Kelchner et al. 1998):

$$\mathrm{CSP} = \sum_{i=1}^{N_p} \left|\mathbf{R}_i + \mathbf{R}_{i+N_p}\right|^2 \tag{13}$$

where $\mathbf{R}_i$ and $\mathbf{R}_{i+N_p}$ are vectors from the considered atom to the i^{th} pair of neighbors, and N_p depends on the crystal structure. For example, $N_p = 6$ for fcc

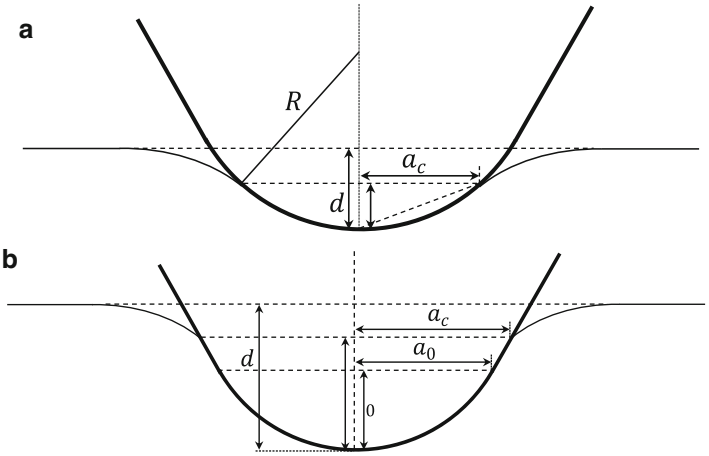

Fig. 1 The true indentation depth h for: **a** spherical part of the indenter **b** conical part of the indenter (Reprinted with permission from Yaghoobi and Voyiadjis 2016a)

materials. *CSP* is equal to zero for perfect crystal structure. However, the atomic vibration introduces a small *CSP* for atoms which are not defects. Accordingly, a cutoff should be introduced in a way that if $CSP_i < CSP_{\text{cutoff}}$, the i^{th} atom is not considered as a defect (Yaghoobi and Voyiadjis 2014). Also, point defect is removed to clearly illustrate stacking faults. Second, the MD outputs can be postprocessed using the Crystal Analysis Tool (Stukowski and Albe 2010; Stukowski 2012, 2014; Stukowski et al. 2012). The common-neighbor analysis method (Faken and Jonsson 1994) is the basic idea of this code. The code is able to calculate the dislocation information such as the Burgers vector and total dislocation length. To extract the required information, the Crystal Analysis Tool constructs a Delaunay mesh which connects all atoms. Next, using the constructed mesh, the elastic deformation gradient tensor is obtained. The code defines the dislocations using the fact that the elastic deformation gradient does not have a unique value when a tessellation element intersects a dislocation.

Boundary Conditions Effects

One of the most important parts of the MD simulation is to select the appropriate boundary conditions which can accurately mimic the considered phenomenon. In the case of nanoindentation, the selected boundary conditions may influence the response of the simulated material. Up to now, four different boundary conditions types have been incorporated in MD to simulate the nanoindentation experiment which can be described as below (Fig. 2):

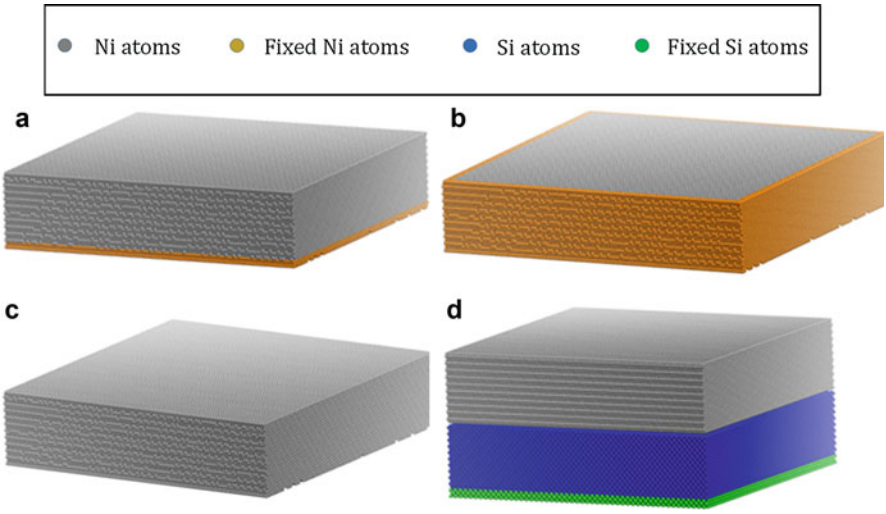

Fig. 2 Boundary conditions of thin films **a** BC1, **b** BC2, **c** BC3, and **d** BC4 (Reprinted with permission from Yaghoobi and Voyiadjis 2014)

- *BC1*: Fixing some atomic layers at the sample bottom to act as a substrate, using free surface for the top, and periodic boundary conditions for the remaining surfaces (see e.g., Nair et al. 2008; Kelchner et al. 1998; Zimmerman et al. 2001)
- *BC2*: Fixing some atomic layer at the surrounding surfaces and using free surfaces for the sample top and bottom (see e.g., Medyanik and Shao 2009; Shao and Medyanik 2010)
- *BC3*: Using free surface for the sample top and bottom, incorporating the periodic boundary conditions for the remaining surfaces, and putting a substrate under the thin film (see e.g., Peng et al. 2010)
- *BC4*: Incorporating the free surfaces for the sample top and bottom, using periodic boundary conditions for the remaining surfaces, and equilibrating the sample by adding some forces (see e.g., Li et al. 2002; Lee et al. 2005)

Yaghoobi and Voyiadjis (2014) studied the different types of boundary conditions and their effects on the dislocation nucleation and evolution patterns using samples with various thicknesses (t_f) indented by spherical indenters with different radii (R). The parallel code LAMMPS (Plimpton 1995), which was developed at Sandia National Laboratories, was selected to conduct the MD simulation. The numerical time integration of Eq. 1 was performed using the velocity Verlet algorithm. Three different types of interatomic interaction were incorporated:

- The interaction of Nickel atoms with each other (Ni-Ni)
- The interaction of Silicon atoms with each other (Si-Si)
- The interaction of Nickel atoms with Silicon ones (Ni-Si)

The three interactions were modeled using the embedded-atom method (EAM) potential for Ni-Ni interaction, Tersoff potential for Si-Si interaction, and Lennard–Jones (LJ) potential for Ni-Si interaction. The Ni-Ni interaction is modeled using the EAM potential parameterized by Mishin et al. (1999). To capture the Si-Si interaction, a three-body Tersoff potential (Tersoff 1988) was chosen. Table 1 presents the potential parameters of Si. The LJ potential E^{LJ} was used to model the Ni-Si interaction and required parameters ($\varepsilon_{\mathrm{Ni-Si}}$ and $\sigma_{\mathrm{Ni-Si}}$) are presented in Table 2. The cutoff distance of 2.5σ was selected for LJ potential. The indenter was spherical modeled using the repulsive force F^{ind} presented in Eq. 8. The centrosymmetry parameter (*CSP*) was incorporated to visualize the defects with the cutoff equal to 1.5 ($CSP_{\mathrm{cutoff}} = 1.5$).

Table 1 Tersoff potential parameters of Si-Si (Yaghoobi and Voyiadjis 2014)

$A = 3264.7$ eV	$B = 95.373$ eV	
$\lambda_1 = 3.2394$ Å^{-1}	$\lambda_2 = 1.3258$ Å^{-1}	
$\alpha = 0$	$\beta = 0.33675$	$n = 22.956$
$c = 4.8381$	$d = 2.0417$	$h = 0.0000$
$\lambda_3 = \lambda_2$	$R = 3.0$ Å	$D = 0.2$ Å

Table 2 LJ potential parameters of Ni-Ni, Si-Si, and Ni-Si (Yaghoobi and Voyiadjis 2014)

	ε (J)	σ (Å)
Ni-Ni	8.3134e-20	2.2808
Si-Si	2.7904e-21	3.8260
Ni-Si	1.5231e-20	3.0534

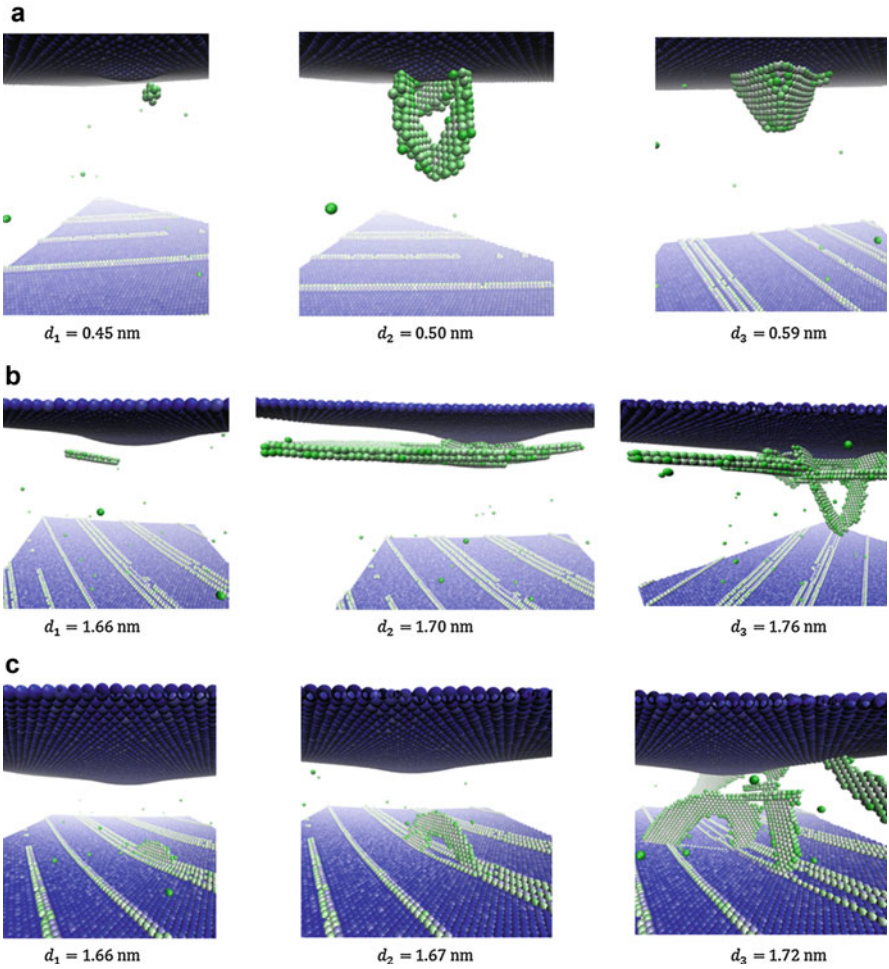

Fig. 3 Defect nucleation and evolution of **a** Type I, **b** Type II, and **c** Type III (Reprinted with permission from Yaghoobi and Voyiadjis 2014)

It was observed that the bending and indentation mechanisms control the initial stages of defect nucleation and evolution for samples with different thicknesses (Yaghoobi and Voyiadjis 2014). Accordingly, three patterns of so-called *Type I*, *Type II*, and *Type III* were observed which can be described as follows (Fig. 3) (Yaghoobi and Voyiadjis 2014):

- *Type I*: The location of initial defect nucleation is beneath the indenter. Two faces of embryonic dislocation loops evolve on $(1\bar{1}1)$ and $(11\bar{1})$ planes. Eventually, a tetrahedral sessile lock is formed. This dislocation pattern is controlled by the indentation mechanism.
- *Type II*: Again, the location of initial nucleation is beneath the indenter. However, the defect evolution occurs on the plane which is parallel to (111), which is the indentation plane. A dislocation pattern similar to *Type I* starts evolving as the indentation depth increases. Both bending and indentation mechanisms are important in this pattern.
- *Type III*: The initial dislocation is nucleated at the sample bottom. The dislocations are evolved on {111} planes while they are moving towards the sample top. Bending is the dominant mechanism of deformation.

Figure 4 presents the nanoindentation responses of samples visualized in Fig. 3. In the case of sample with *Type I* defect structure pattern, the first load relaxation occurs due to the initial defect nucleation beneath the indenter (Fig. 4a). Two faces of embryonic dislocation loops evolve on $(1\bar{1}1)$ and $(11\bar{1})$ planes. Another load relation occurred when the tetrahedral sessile lock is shaped. Figure 4b illustrates the effects of defect evolution on the response of the sample with dislocation pattern of *Type II* during nanoindentation. The indentation force is initially relaxed due to the first defect nucleation beneath the indenter. The defect evolution occurs on the plane which is parallel to (111), which is the indentation plane. Due to the complexity of dislocation evolution pattern and activation of both bending and indentation mechanisms, the effects of defects pattern on the nanoindentation response become complicated. Figure 4c shows that indentation load is initially released due to the first dislocation nucleation at the bottom for sample with *Type III* pattern. After the initial load relaxation, the complex pattern of dislocation nucleation and evolution leads to the oscillatory response. However, the general trend is the indentation load increases during indentation.

The governing mechanisms of deformation also depend on the film thickness t_f and indenter radius R (Yaghoobi and Voyiadjis 2014). Samples with BC1 experience no bending independent of the film thickness or indenter radius which leads to the *Type I* pattern controlled by indentation mechanism. Sample with BC2 and BC3 may experience all the patterns of *Type I*, *Type II*, and *Type III* depending on the value of R/t_f. For very small values of R/t_f, the indentation governs the deformation mechanism and *Type I* pattern occurs. Increasing R/t_f, bending mechanism also becomes important and *Type II* pattern occurs. Further increasing R/t_f leads to the *Type III* pattern which is governed by the bending mechanism.

The contact pressure at the onset of plasticity p_m^y is one of the properties which is commonly investigated during nanoindentation. Yaghoobi and Voyiadjis (2014) showed that the p_m^y is also influenced by the choice of MD boundary conditions. The effect can be predicted using the pattern of dislocation nucleation and evolution. In the case of *Type I* pattern, p_m^y is independent of film thickness. However, p_m^y depends on the film thickness for samples with *Type II* and *Type III* in a way that p_m^y increases by increasing the film thickness. Comparing the dislocation nucleation and evolution

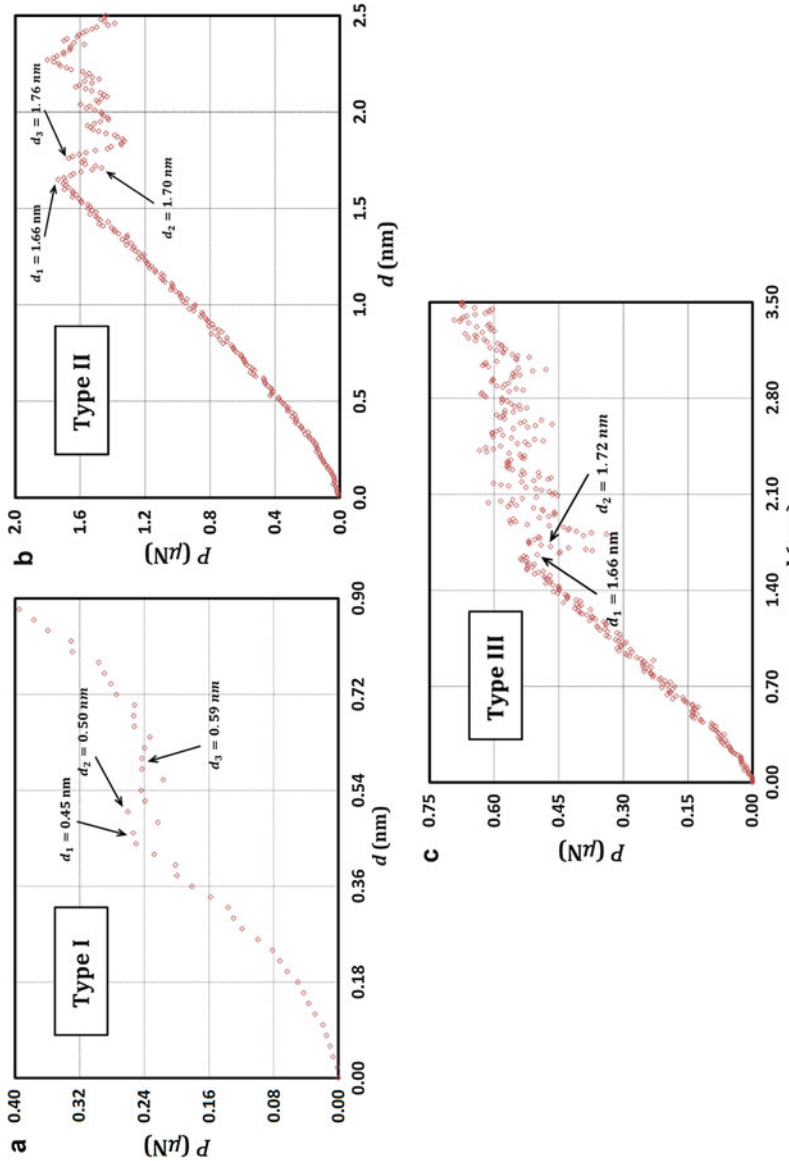

Fig. 4 Nanoindentation responses of thin films with different dislocation nucleation patterns of **a** Type I, **b** Type II, and **c** Type III (Reprinted with permission from Yaghoobi and Voyiadjis 2014)

pattern with each other, *Type I* has the largest and *Type III* has the smallest contact pressure at the time of plasticity initiation.

Comparing MD Results with Theoretical Models

Several theoretical models have been proposed to predict the variation of dislocation length during nanoindentation experiment. Nix and Gao (1998) predicted the variation of geometrically necessary dislocations (GNDs) by integrating the dislocation loops induced during nanoindentation. The dislocation length produced during nanoindentation using a conical indenter can be described as follows (Nix and Gao 1998; Swadener et al. 2002):

$$\lambda_{\text{co}} = \frac{\pi a_c h}{b} \tag{14}$$

Pugno (2007) generalized the method by replacing the surface of indentation with the staircase-like surface and presented a generalized equation for dislocation length prediction:

$$\lambda = \frac{S}{b} \tag{15}$$

where $S = \Omega - A$ and Ω is the total contact surface. The variation of dislocation length during nanoindentation using cylindrical and right square prismatic indenters can be obtained using Eq. 15 as below:

$$\lambda_{\text{cy}} = \frac{2\pi a_c h}{b} \tag{16}$$

$$\lambda_{\text{pr}} = \frac{4\text{ch}}{b} \tag{17}$$

where b is the magnitude of the Burgers vector and $c = \sqrt{A}$.

Voyiadjis and Yaghoobi (2015) conducted MD simulation of Ni thin film during nanoindentation to investigate the proposed theoretical models for dislocation length using different indenter geometries of right square prismatic, conical, and cylindrical. The Ni thin film dimensions were 1,200 nm, 1,200 nm, and 600 nm along $[1\bar{1}0]$, $[11\bar{2}]$, and [111] directions, respectively. The radius of cylindrical indenter was $r_1 = 4.8$ nm. The indentation surface of the right square prismatic indenter was a 7.5×7.5 nm^2. The smaller radius of blunt conical indenter was $r_2 = 0.3$ nm with the cone semi-angle of $\theta = 56.31°$. The parallel code LAMMPS (Plimpton 195) was selected to conduct the MD simulation. The numerical time integration was performed using the velocity Verlet algorithm. *BC4* was incorporated for MD simulation of nanoindentation. The EAM potential is used for Ni-Ni interaction which was parameterized by Mishin et al. (1999). The indenter was modeled

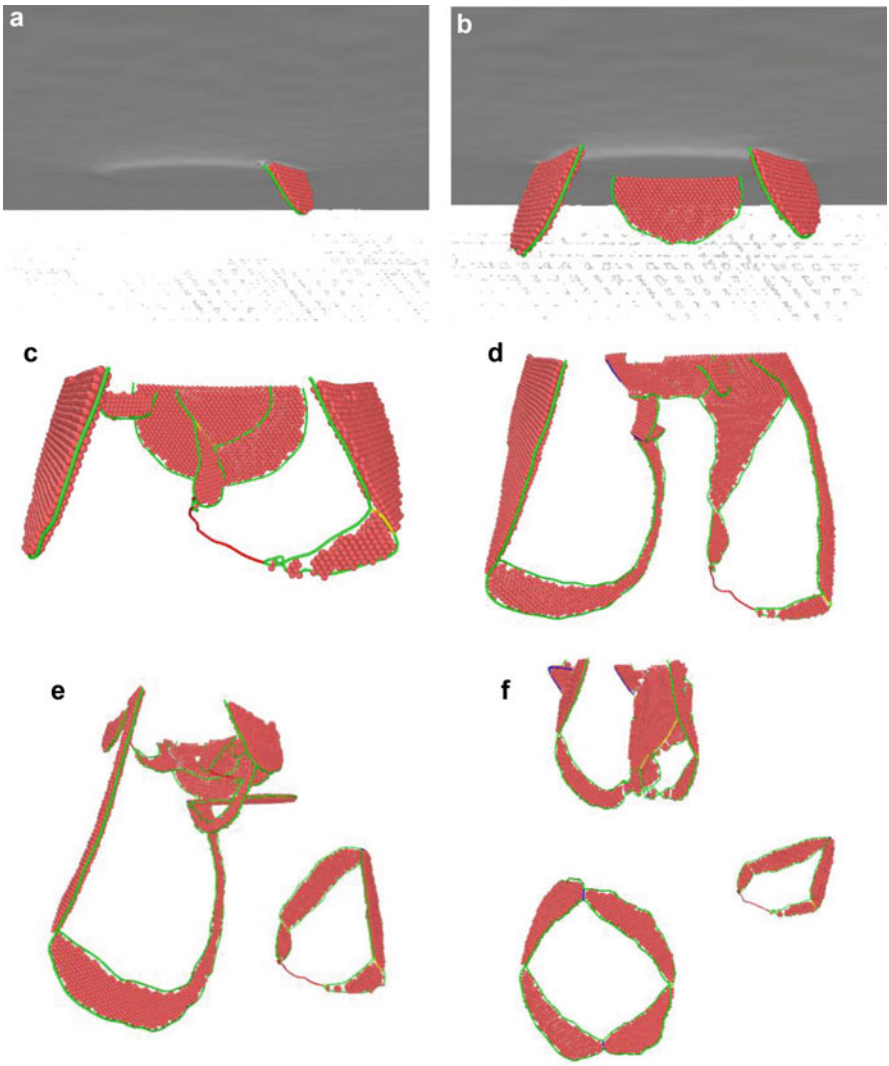

Fig. 5 Defect nucleation and evolution of Ni thin film indented by the cylindrical indenter at **a** $d \approx 0.70$ nm **b** $d \approx 0.86$ nm **c** $d \approx 0.96$ nm **d** $d \approx 1.02$ nm **e** $d \approx 1.05$ nm **f** $d \approx 1.12$ nm (Reprinted with permission from Voyiadjis and Yaghoobi 2015)

using the repulsive potential E^{ind} presented in Eq. 9. The dislocation was extracted from atomistic data using the Crystal Analysis Tool (Stukowski and Albe 2010; Stukowski 2012, 2014; Stukowski et al. 2012).

First, Voyiadjis and Yaghoobi (2015) investigated the dislocation nucleation and evolution pattern during nanoindentation. As an example, Fig. 5 shows the dislocation nucleation and evolution for Ni thin film indented by a cylindrical indenter during nanoindentation. The dislocations and stacking faults are visualized

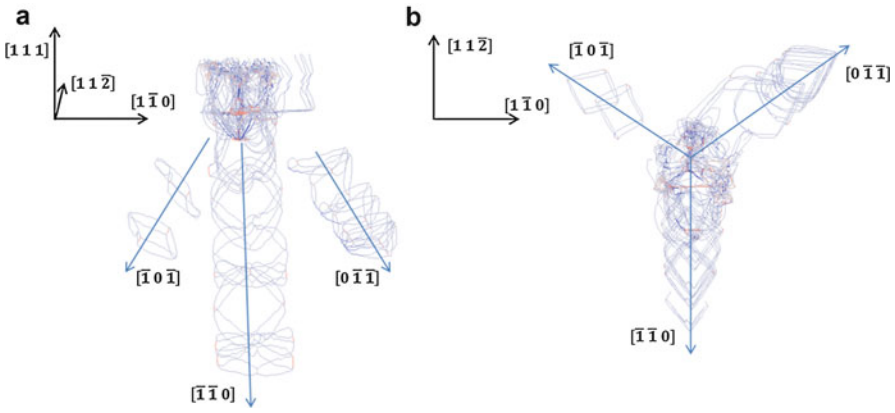

Fig. 6 Prismatic loops forming and movement in Ni thin film indented by the cylindrical indenter during nanoindentation **a** side view **b** top view (Reprinted with permission from Voyiadjis and Yaghoobi 2015)

while the perfect atoms are removed. The color of Shockley, Hirth, and stair-rod partial dislocations and perfect dislocations are green, yellow, blue, and red, respectively. Figure 6 illustrates the dislocation loop formation and movement along three directions of $[\bar{1}\,0\bar{1}]$, $[\bar{1}\bar{1}0]$, and $[0\bar{1}\bar{1}]$. Figure 7 compares the dislocation lengths obtained from atomistic simulation with those predicted by Eqs. 14–17. The results show that the theoretical predictions can accurately capture the dislocation lengths during nanoindentation. However, some discrepancies are observed which can be described as follows:

- Atomistic simulation captures the total dislocation length including both geometrically necessary and statistically stored dislocations, while the theoretical models only calculate geometrically necessary dislocations. This is the reason that the MD simulation dislocation lengths are mostly higher than that of the theoretical ones.
- The theoretical models incorporate the Burgers vector of the Shockley partial dislocations which comprised most of the dislocation content. However, a few stair-rod and Hirth partial and perfect dislocations are nucleated with the Burgers vectors different from the one for Shockley partial dislocations.
- The dislocations which are detached from the main dislocations network as the prismatic loops and leave the plastic zone around the indenter are not considered in the total dislocation length calculation.

Size Effects in Small-Length Scales During Nanoindentation

Demir et al. (2009) observed that the governing mechanisms of size effects at smaller length scales are not similar to those of the large size samples during nanoindentation. They observed that increasing the dislocation density decreases

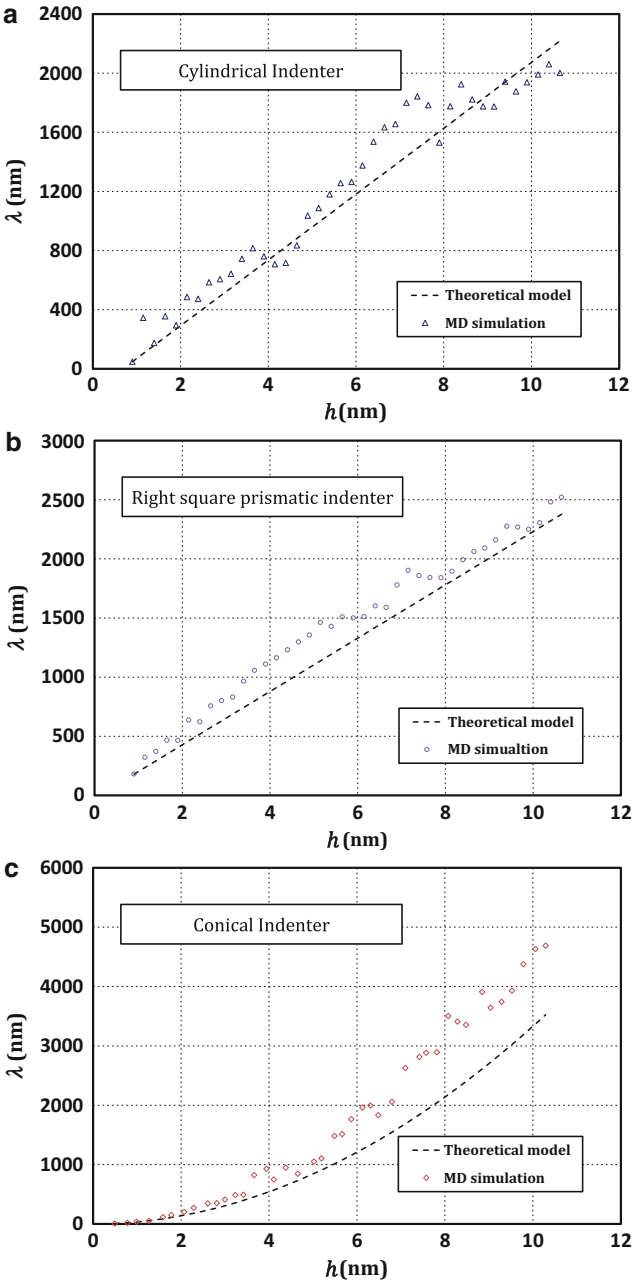

Fig. 7 Total dislocation length obtained from simulation and theoretical models in samples indented by the **a** cylindrical indenter **b** *right square* prismatic indenter **c** conical indenter (Reprinted with permission from Voyiadjis and Yaghoobi 2015)

the strength (Demir et al. 2009). Uchic et al. (2009), Kraft et al. (2010), and Greer (2013) reviewed the different sources of size effects occurring at smaller length scales. Three mechanisms of source exhaustion, source truncation, and weakest link theory have been introduced to capture the size effects. In samples with very small length scales, lacking enough dislocations to sustain the imposed plastic flow leads to the strength enhancement which is commonly termed as source exhaustion hardening (Rao et al. 2008; El-Awady 2015). The dislocation content reduction may happen due to dislocation starvation, i.e., when the dislocations escape from the sample free surfaces, mechanical annealing, or dislocation source shut down. The material strength also depends on the length of dislocation sources in a way that decreasing the length of dislocation source increases the strength. The dislocation source length becomes smaller by decreasing the sample size through a procedure so-called source truncation. In this procedure, the double-ended dislocation sources transform to a single-ended ones due to the surface effects which decreases the length of dislocation sources. Accordingly, decreasing the sample size leads to a smaller single-ended dislocation source which enhances the material strength (Parthasarathy et al. 2007; Rao et al. 2007). The weakest link theory states that the material strength increases by decreasing the sample size, because decreasing the sample length scale will increase the strength of the weakest source available in the sample (Norfleet et al. 2008; El-Awady et al. 2009).

Yaghoobi and Voyiadjis (2016a) incorporated the large scale MD to study the sources of size effects at smaller length scales during nanoindentation. They selected single crystal Ni thin films with the dimensions of 120 nm, 120 nm, and 60 nm along $[1\bar{1}0]$, $[11\bar{2}]$, and [111] directions, respectively. A conical indenter with a spherical tip was incorporated which is similar to the one used by Demir et al. (2009). The remaining simulation methodology is similar to the section "Comparing MD Results with Theoretical Models."

Swadener et al. (2002) approximated the spherical indenter geometry with a parabola and presented the following equation to predict the GNDs length during nanoindentation:

$$\lambda_{\mathrm{sp}} \approx \frac{2\pi}{3}\frac{a_c^3}{\mathrm{bR}} \tag{18}$$

The approximation, however, is only applicable for small indentation depths. Yaghoobi and Voyiadjis (2016a) introduced a theoretical equation to predict the dislocation length of sample indented by a spherical tip using the precise geometry of the indenter. The total dislocation length can be described as below (Yaghoobi and Voyiadjis 2016a):

$$\begin{aligned}\lambda_{\mathrm{sp}} &= \int_0^{a_c} \frac{2\pi r}{b}\left(\frac{\mathrm{dh}}{\mathrm{dr}}\right)\mathrm{dr} = \frac{2\pi}{b}\int_0^{a_c}\left(\frac{r^2}{\sqrt{R^2-r^2}}\right)\mathrm{dr} \\ &= \frac{2\pi}{b}\left[\frac{R^2}{2}\sin^{-1}\left(\frac{a_c}{R}\right) - \frac{1}{2}\left(a_c\sqrt{R^2-{a_c}^2}\right)\right]\end{aligned} \tag{19}$$

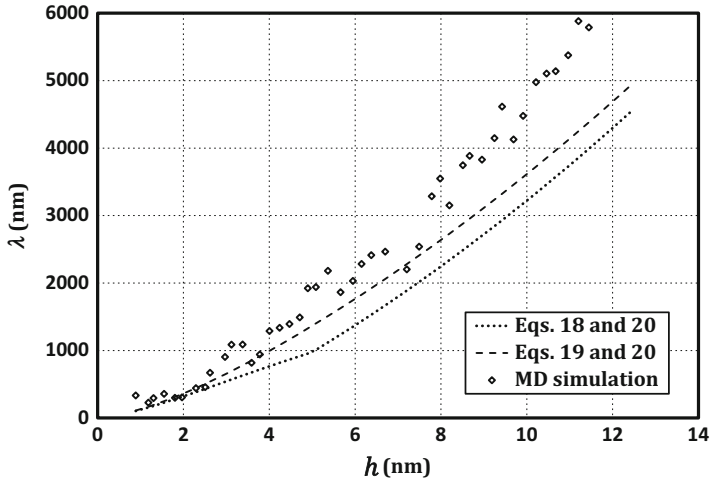

Fig. 8 Comparison between the dislocation lengths obtained from theoretical models and MD simulation during nanoindentation (Reprinted with permission from Yaghoobi and Voyiadjis 2016a)

The GNDs length for the conical part of the indenter can be calculated as below:

$$\lambda_{\mathrm{co}} = \lambda_{\mathrm{sp}}\big|_{h=h_0} + \int_{a_0}^{a_c} \frac{2\pi r}{b\tan\left(\frac{\theta}{2}\right)}\mathrm{dr} = \lambda_{\mathrm{sp}}\big|_{h=h_0} + \frac{\pi\left({a_c}^2 - {a_0}^2\right)}{b\tan\left(\frac{\theta}{2}\right)} \tag{20}$$

Figure 8 compares the dislocation length obtained from atomistic simulation with those calculated from the approximate and precise theoretical models during nanoindentation. The GNDs length calculated from the theoretical model is a lower bound for the total dislocation length obtained from MD which includes all types of dislocations.

A plastic zone should be defined to obtain the dislocation density. Yaghoobi and Voyiadjis (2016a) assumed that the plastic zone is a hemisphere with the radius of $R_{\mathrm{pz}} = \mathrm{f}a_c$ where f is a constant. The value of $f = 1.9$ was selected by Yaghoobi and Voyiadjis (2016a) for the theoretical dislocation density calculations which is similar to Durst et al. (2005). The density of dislocations can be described as below:

$$\rho = \lambda / V \tag{21}$$

where V is the plastic zone volume. Figure 9 compares the approximate and precise theoretical dislocation densities. Figure 9 shows that approximating a sphere using a parabola leads to a constant dislocation density. However, the density of dislocations increases during nanoindentation by incorporating the precise indenter geometry.

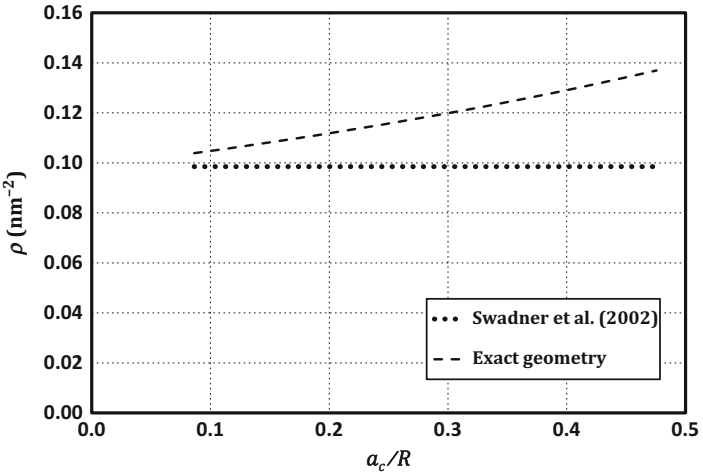

Fig. 9 Theoretical GNDs density obtained from the approximate (Swadener et al. 2002) and exact (see Eq. 19) geometries of the indenter versus the normalized contact radius a_c/R (Reprinted with permission from Yaghoobi and Voyiadjis 2016a)

Yaghoobi and Voyiadjis (2016a) incorporated five different values of $f = 1.5$, 2.0, 2.5, 3.0, and 3.5 and obtained the corresponding dislocation density for each one. The volume of plastic zone can be obtained by removing the volume occupied by the indenter (V_{indenter}) as follows:

$$V = (2/3)\,\pi\,(\text{fa}_c)^3 - V_{\text{indenter}} \tag{22}$$

Figure 10 illustrates the variation of dislocation density ρ during nanoindentation for different sizes of plastic zone. The results show that for all values of f, the dislocation density increases during nanoindentation which is in agreement with the trend predicted by the precise theoretical prediction presented in Fig. 9.

Figure 11 presents the variation of the mean contact pressure ($p_m = P/A$), which is equivalent to the hardness H in the plastic region, during nanoindentation. Figure 11 shows that the mean contact pressure follows the Hertzian theory in the elastic region. After the initial dislocation nucleation, however, the results show that the hardness decreases by increasing the indentation depth.

The forest hardening mechanism governs the material strength in bulk-sized samples which relate the material strength to the interaction of dislocations with each other. The famous Taylor hardening-type models are usually incorporated to describe the shear strength in the case of forest hardening mechanism as follows (Voyiadjis and Al-Rub 2005):

$$\begin{aligned} \tau &= \alpha_S \mu b_S \sqrt{\rho} \\ \rho &= \left[\rho_S^{\beta/2} + \left(\alpha_G^2 b_G^2 \rho_G / \alpha_S^2 b_S^2\right)^{\beta/2}\right]^{2/\beta} \end{aligned} \tag{23}$$

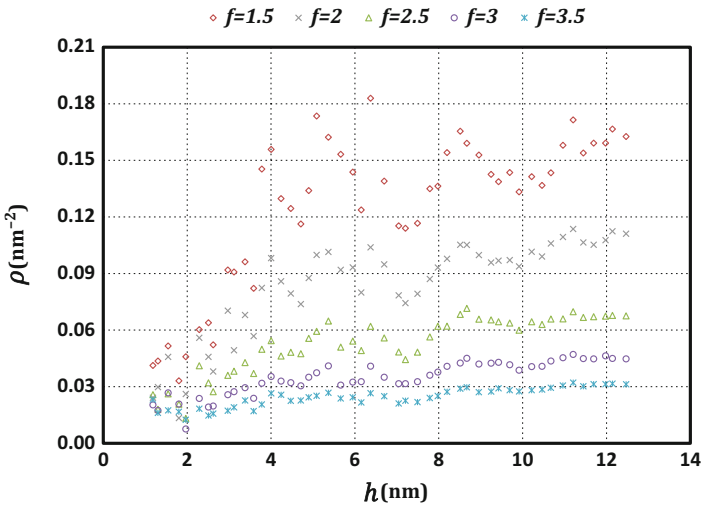

Fig. 10 Dislocation density obtained from MD simulation for different values of f during nanoindentation (Reprinted with permission from Yaghoobi and Voyiadjis 2016a)

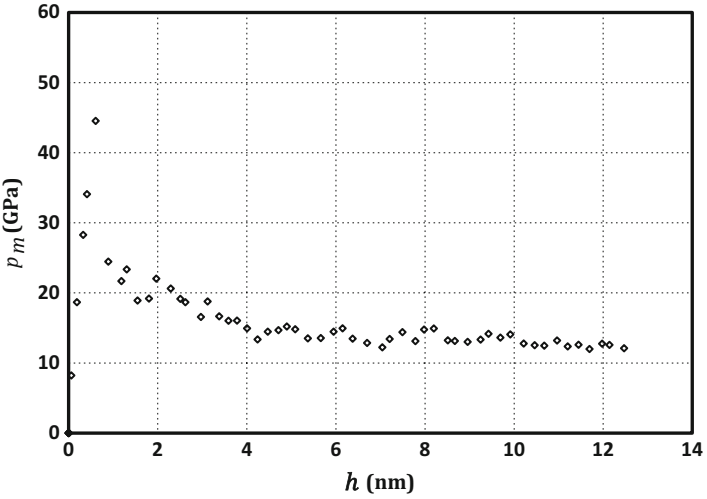

Fig. 11 Variation of mean contact pressure p_m as a function of indentation depth h (Reprinted with permission from Yaghoobi and Voyiadjis 2016a)

where α is a constant, μ is the shear modulus, and the indices G and S designate GNDs and SSDs parameters, respectively. Equation 23 states the material strength increases by increasing the dislocation density. Figure 10 shows that the dislocation density increases by increasing the indentation depth. According to the forest hardening mechanism, the strength should also increase. However, Fig. 11 illustrates

that the hardness decreases during nanoindentation, and the material size effects cannot be captured by the forest hardening mechanism.

The dislocation nucleation and evolution should be investigated in addition to the nanoindentation response to unravel the controlling mechanisms of size effects. Figure 12 depicts the initial stages of dislocation evolution. It shows that the cross-slip is the dominant mechanism to produce the dislocation sources. Elongation of dislocations pinned at their ends provides the required dislocation length to

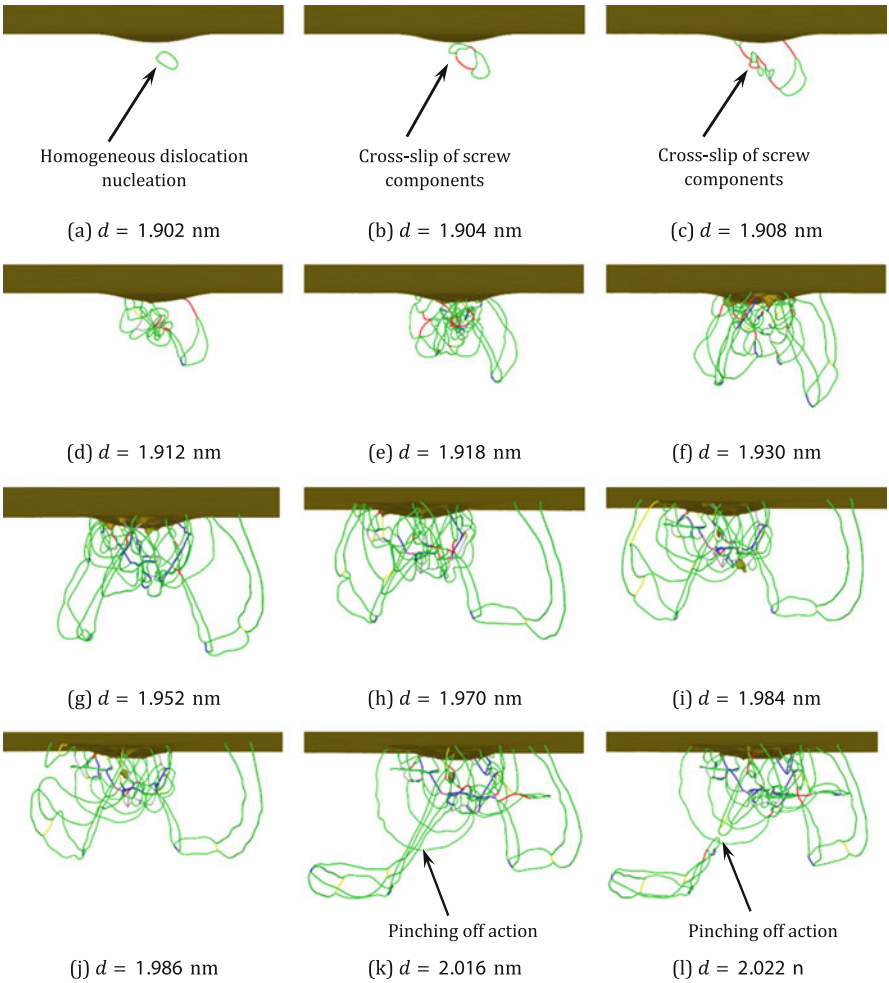

Fig. 12 Dislocation nucleation and evolution at small tip displacements: **a** initial homogeneous dislocation nucleation beneath the indenter which has a Burgers vector of $1/6\left[\bar{2}11\right]$ (Shockley partial dislocation); **b–j** cross-slip of screw components which produces new pinning points; **k–l** first loop is released by pinching off action (Reprinted with permission from Yaghoobi and Voyiadjis 2016a)

sustain the imposed deformation. Dislocation loops are then released by pinching off of screw dislocations and glide along the three directions of $[\bar{1}10]$, $[0\bar{1}1]$, and $[\bar{1}\,0\bar{1}]$. After the initial dislocation nucleation, the available dislocation length is insufficient to sustain the imposed deformation, and the source exhaustion controls the size effects. Consequently, the required stress reduces as the dislocation length and density increase during nanoindentation. The dislocation density and length are eventually reaching the value required to sustain the imposed plastic flow, and the hardness tends to a constant value. Also, the interaction of dislocation with each other becomes important by increasing the dislocation length. However, the dislocation density reaches a constant value and forest hardening mechanism does not lead to any size effects.

Effects of Grain Boundary on the Nanoindentation Response of Thin Films

Grain boundary (GB) has a key role in deformation mechanism of crystalline material (Meyers et al. 2006; Koch et al. 2007; Zhu et al. 2008). For crystalline materials with large grains, the Hall-Petch relation describes the effects of grain size which states the material strength increases by decreasing the grain size. Hall-Petch effect is commonly attributed to the dislocation pile-up mechanism (Meyers et al. 2006; Koch et al. 2007; Zhu et al. 2008). The Hall-Petch relation breaks down for grain size smaller than some limits, and other deformation mechanisms control the size effects in crystalline materials such as the grain boundary rotation and sliding (Meyers et al. 2006; Koch et al. 2007; Zhu et al. 2008).

Atomistic simulation is a powerful tool to study the interaction of dislocations with GBs. Several mechanisms of dislocation reflection, transmission, and absorption were investigated by De Koning et al. (2003) by incorporating the atomistic simulation. Hasnaoui et al. (2004) studied the interaction between the dislocations and GB during nanoindentation experiment using molecular dynamics. Jang and Farkas (2007) conducted the atomistic simulation of bicrystal nickel thin film nanoindentation and observed that the GBs can contribute to the nanoindentation hardness. Kulkarni et al. (2009), however, observed that the GBs mainly reduce the hardness of the metallic samples. They showed that the CTB has the least hardness reduction compared to the other types of GBs (Kulkarni et al. 2009). Tsuru et al. (2010) investigated the effect of indenter distance from the GB using MD. Stukowski et al. (2010) conducted MD simulation of nanoindentation for metallic samples with twin boundaries and observed that the effects of twin GBs on the material response depends on the unstable stacking fault and twin boundary migration energies. Sangid et al. (2011) proposed an inverse relation between the GB energy barrier and GB energy based on the MD simulation results.

Effects of GB on the response of thin film during nanoindentation has been studied by many researchers (Hasnaoui et al. 2004; Jang and Farkas 2007; Kulkarni et al. 2009; Tsuru et al. 2010). However, a study which

addresses a wide range of grain sizes is not a trivial task due to the MD simulation limitations. Voyiadjis and Yaghoobi (2016) incorporated the large-scale MD to study the effects of grain size and grain boundary geometry on the nanoindentation response. They incorporated Ni thin films with two sizes of $24 \times 24 \times 12$ nm (S1) and $120 \times 120 \times 60$ nm (S2). Four symmetric tilt boundaries of $\sum 3(111)\ [1\bar{1}0]\ \left(\theta = 109.5^{\circ}\right)$, $\sum 11(113)\ [1\bar{1}0]\ \left(\theta = 50.5^{\circ}\right)$, $\sum 3\,(1\,1\,2)\ [1\bar{1}0]\ \left(\theta = 70.5^{\circ}\right)$, and $\sum 11(332)\ [1\,\bar{1}\,0]\ \left(\theta = 129.5^{\circ}\right)$ and three asymmetric tilt boundaries of $\sum 11$ (225)/(441) ($\varphi = 54.74^{\circ}$), $\sum 3\,(112)/\,(\bar{5}\bar{5}2)\ \left(\varphi = 19.47^{\circ}\right)$, and $\sum 3\,(114)/(110)\,(\varphi = 35.26^{\circ})$ were generated at the two third of the sample from bottom to compare the governing mechanisms of size effects with those of the single crystal thin films. θ and φ are the interface misorientation and inclination angles, respectively. The spherical indenters with two different radii of $R_1 = 10$ nm and $R_2 = 15$ nm were modeled using the repulsive potential E^{ind} presented in Eq. 9. The procedure to generate and equilibrate the GBs was elaborated by Voyiadjis and Yaghoobi (2016). The equilibrium structures of grain boundaries are illustrated in Fig. 13 using the *CSP*. The remaining simulation methodology is similar to the section "Comparing MD Results with Theoretical Models."

Figure 14 depicts the variation of mean contact pressure p_m during nanoindentation for S1 thin films, i.e., the smaller samples. It can be observed that the GB generally reduces the material strength for S1 thin films. However, in the case of coherent twin boundary (CTB), i.e., $\sum 3\ (111)\ [1\bar{1}0]$, the hardness is slightly enhanced for some indentation depths. Generally, in the cases of smaller thin films, i.e., S1 samples, the CTB has the best performance. Further investigation was conducted by depicting the variation of dislocation length λ during nanoindentation. Figure 15 illustrates the variation of p_m and λ during nanoindentation for CTB. Voyiadjis and Yaghoobi (2016) divided the nanoindentation response to five different regions:

- *Region I*: The bicrystal and single crystal thin films show similar responses during the initial indentation phase which are elastic, and CTB is the only defect that exists in the bicrystal thin film.
- *Region II*: In this region, the dislocation nucleation occurs for the bicrystal thin film beneath the indenter followed by a stress relaxation while the single crystal sample remains elastic. In the case of bicrystal thin film, the size effects is initially governed by the dislocation nucleation and source exhaustion. The dislocation density increases during nanoindentation which decreases the required stress to sustain the imposed plastic flow. Consequently, the hardness decreases by nucleation and evolution of new dislocations.
- *Region III*: The plasticity is initiated in single crystal thin film beneath the indenter followed by a stress relaxation. The thin film strength reduces according to the dislocation nucleation and source exhaustion mechanisms. The dislocation content does not change for bicrystal thin film. Accordingly, the stress should

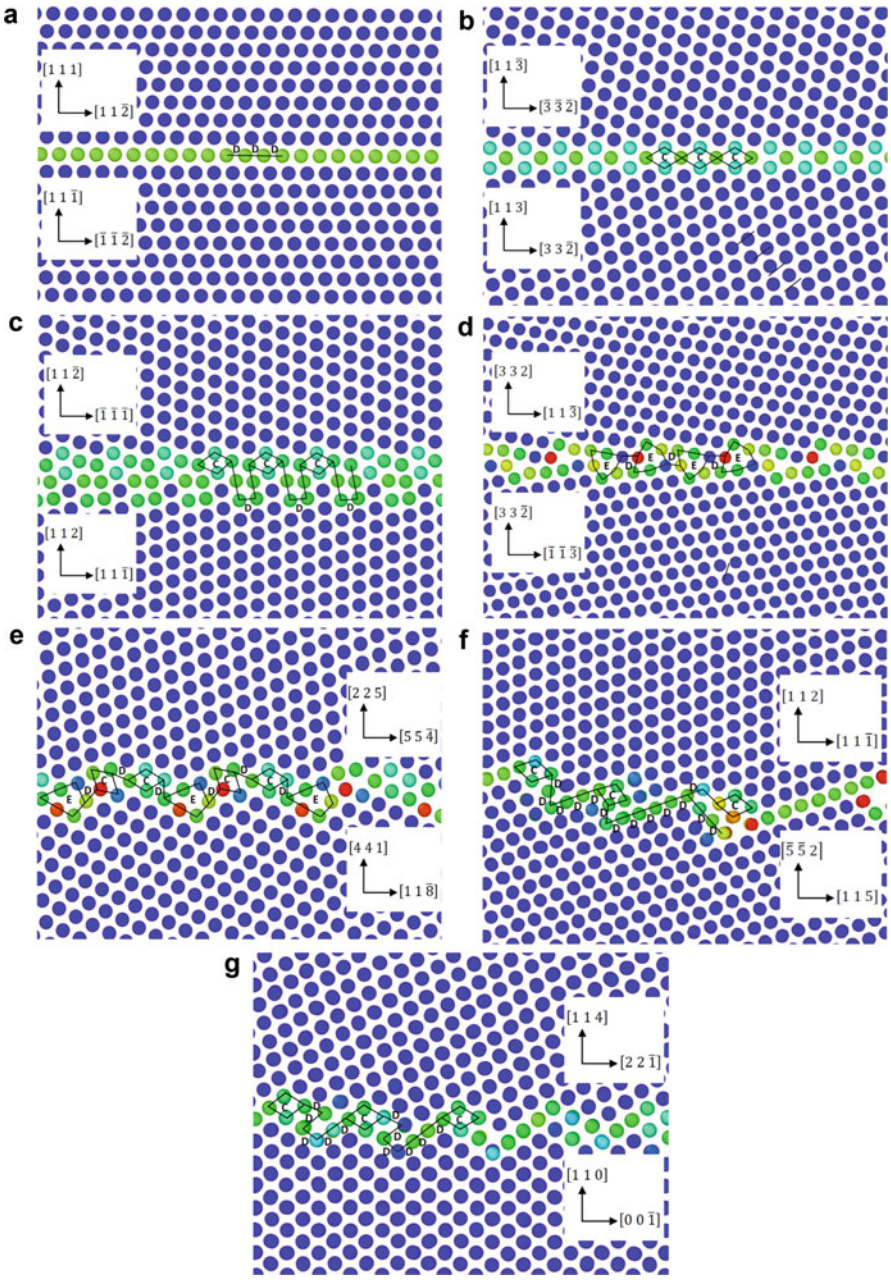

Fig. 13 The equilibrium structure of the symmetric and asymmetric tilt grain boundaries of **a** $\sum 3(111)\ [1\bar{1}0]$ ($\theta = 109.5^{\circ}$), **b** $\sum 11(113)\ [1\bar{1}0]$ ($\theta = 50.5^{\circ}$) $\sum 3(1\ 1\ 2)$, **c** $[1\bar{1}0]$ $\left(\theta = 70.5^{\circ}\right)$, **d** $\sum 11(332)\ [1\ \bar{1}\ 0]$ $\left(\theta = 129.5^{\circ}\right)$, **e** $\sum 11\ (225)/(441)$ ($\varphi = 54.74^{\circ}$), **f** $\sum 3\ (112)/(\bar{5}\bar{5}2)$ $\left(\varphi = 19.47^{\circ}\right)$, and **g** $\sum 3\ (114)/(110)$ ($\varphi = 35.26^{\circ}$), along $[1\bar{1}0]$ axis (Reprinted with permission from Voyiadjis and Yaghoobi 2016)

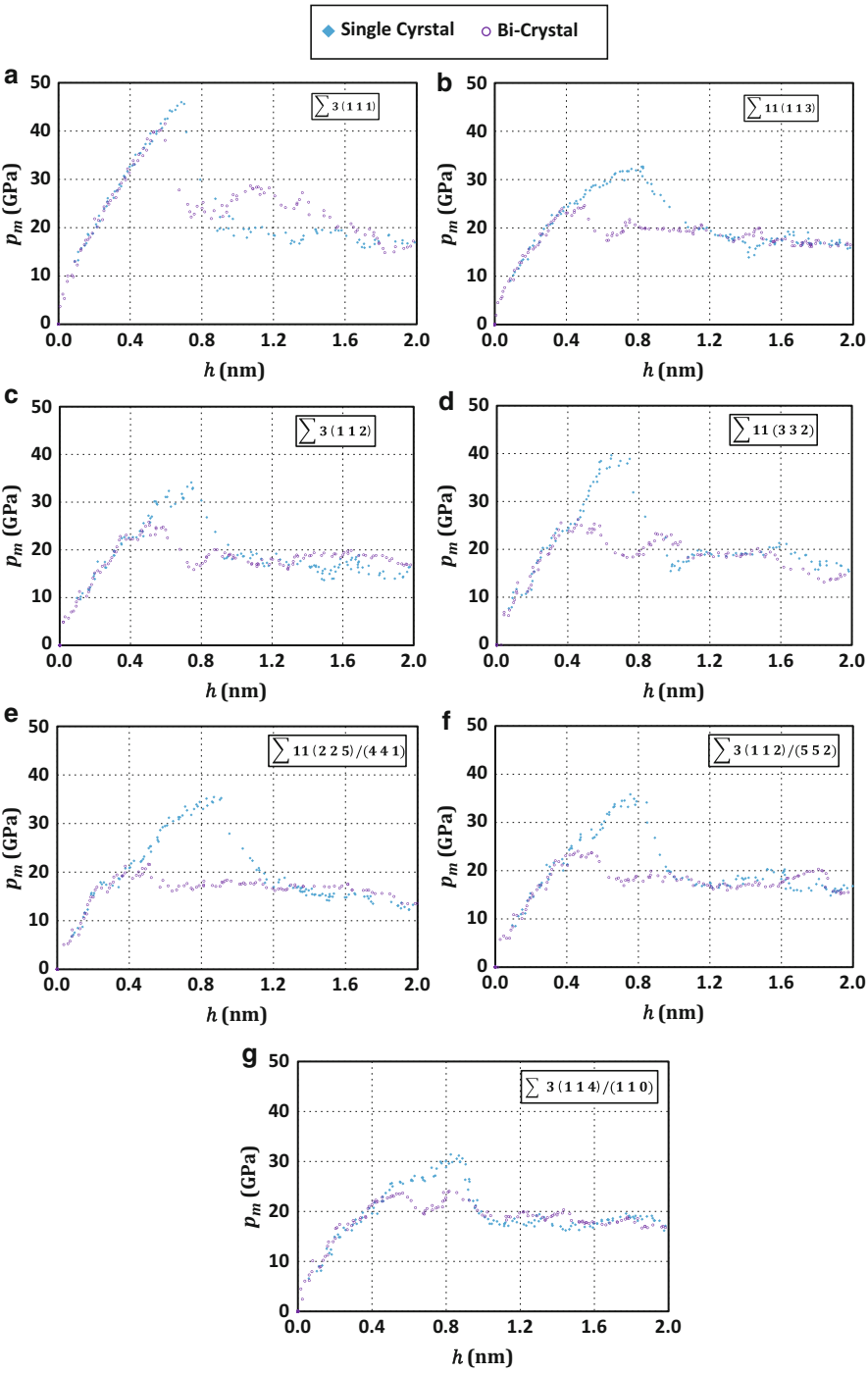

Fig. 14 Variation of mean contact pressure p_m as a function of indentation depth h for S1 single crystal and their related bicrystal samples with the grain boundaries of **a** $\sum 3(111)$, **b** $\sum 11(113)$, **c** $\sum 3(112)$, **d** $\sum 11(332)$, **e** $\sum 11(225)/(441)$, **f** $\sum 3\,(112)/\,(\bar{5}\bar{5}2)$, and **g** $\sum 3(114)/(110)$ (Reprinted with permission from Voyiadjis and Yaghoobi 2016)

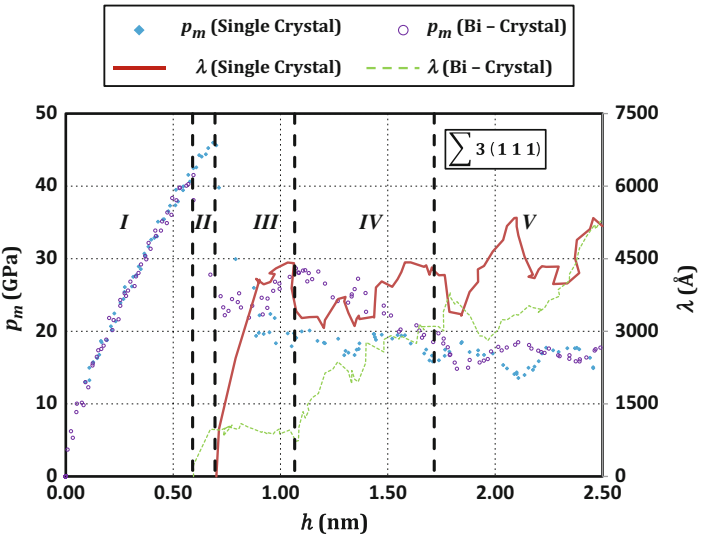

Fig. 15 Variation of mean contact pressure p_m and dislocation length λ as a function of indentation depth h for S1 bicrystal sample with $\sum 3(111)$ GB and its related single crystal sample (Reprinted with permission from Voyiadjis and Yaghoobi 2016)

be increased to sustain the imposed deformation based on the source exhaustion mechanism. The dislocations eventually reach the GB which blocks the dislocations. However, the blocked dislocations do not contribute to the strength.

- *Region IV*: The strength in both single and bicrystal thin films is decreased by increasing the dislocation length which follows the source exhaustion mechanism. However, the influence of the source exhaustion mechanism decreases as the dislocation length increases which decreases the slope of the hardness reduction. Also, the dislocations which are blocked by the GB start dissociating into the next grain.
- *Region V:* In this region, the available dislocation content is sufficient to sustain the imposed plastic flow and no further stress reduction occurs. Also, the single and bicrystal thin films reach a similar hardness which shows that the dislocation blockage by GB does not have any contribution to the size effects.

The structures of dislocations in different regions are illustrated in Fig. 16 for bicrystal thin film with CTB and related single crystal sample. Figure 16a, b shows the dislocation structure in *Region II* at which the single crystal sample is defect free and the nucleation occurs beneath the indenter for bicrystal thin film. The results show that the dominant mechanism of dislocation multiplication is cross-slip. Cross-slip introduces the new pinning points and provides the required dislocation length to sustain the plastic flow. Dislocations are elongated while they are pinned at their ends. Figure 16c, d illustrates the dislocation structure in *Region III* while the cross-slip is still the governing mechanism of deformation for both single and

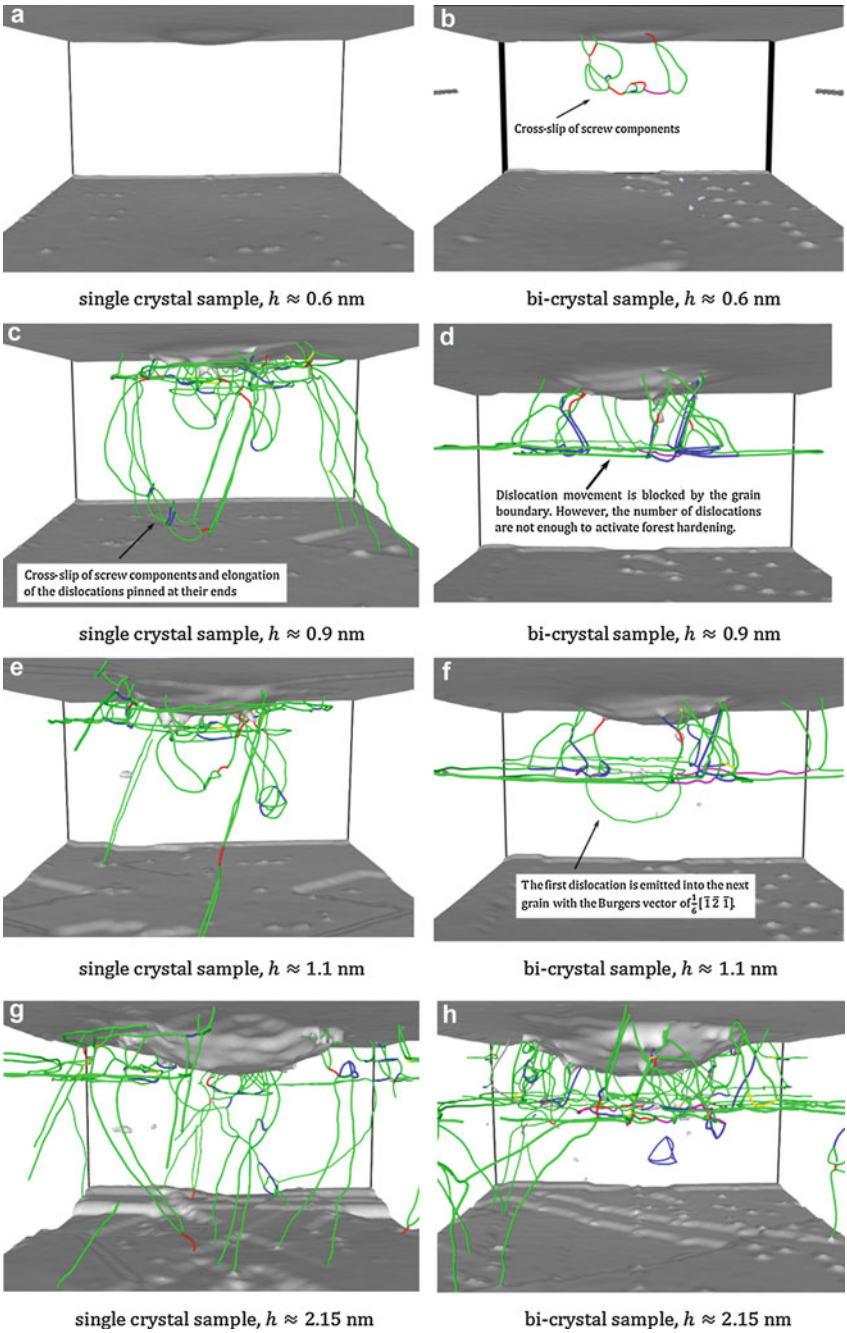

Fig. 16 Dislocation nucleation and evolution: **a** *Region II*, single crystal sample; **b** *Region II*, bicrystal sample; **c** *Region III*, single crystal sample; **d** *Region III*, bicrystal sample; **e** *Region IV*, single crystal sample; **f** *Region IV*, bicrystal sample; **g** *Region V*, single crystal sample; **h** *Region V*, bicrystal sample (Reprinted with permission from Voyiadjis and Yaghoobi 2016)

bicrystal thin films. Figure 16d depicts the dislocation blockage by CTB. Figure 16e, f illustrates the dislocation structure in *Region IV*. Many dislocation multiplications are observed in both single and bicrystal thin films which are induced according to the cross-slip mechanism. Figure 16f shows the initial dislocation dissociation into the next grain in the case of bicrystal sample which is a Shockley partial dislocation with the Burgers vector of $\frac{1}{6}\left[\overline{121}\right]$. In the case of *Region V*, Fig. 16g, h depicts the dislocation structure which shows enough dislocation length is provided to sustain the imposed deformation. Also, the interaction of dislocations with each other cannot be neglected anymore.

Figure 17 shows the variation of p_m and λ during nanoindentation for the S1 samples with different GBs and their related single crystal thin films. In contrast to

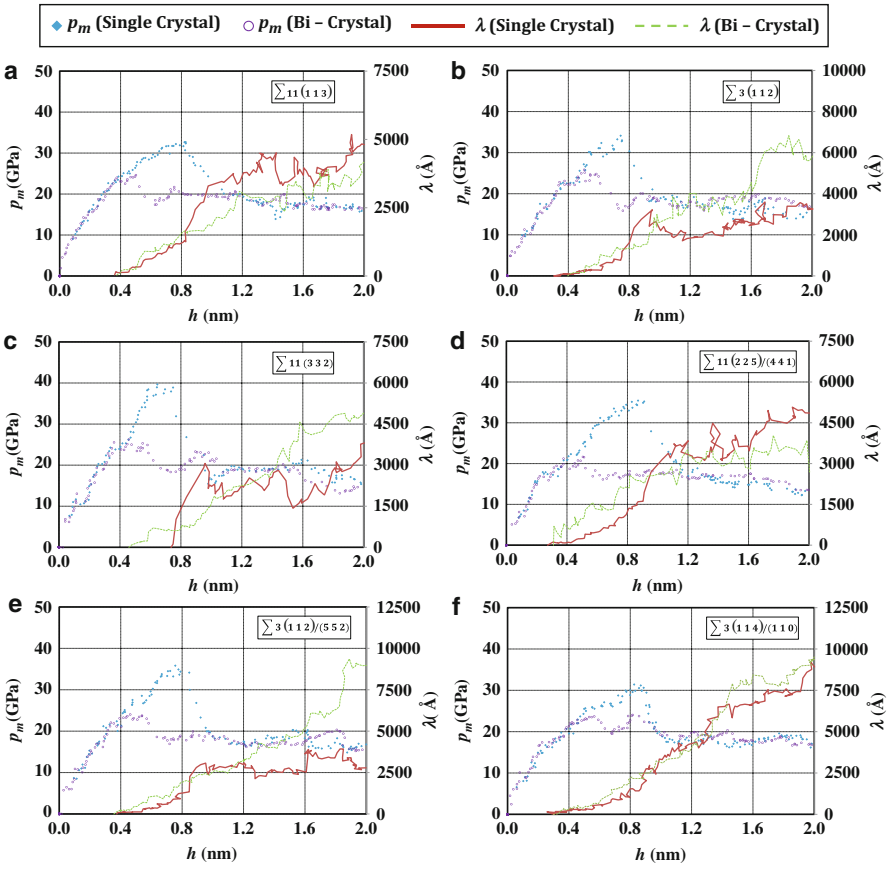

Fig. 17 Variation of mean contact pressure p_m and dislocation length λ as a function of indentation depth h for S1 bicrystal and their related single crystal samples with grain boundaries of: **a** $\sum$11(113), **b** $\sum$3(112), **c** $\sum$11(332), **d** $\sum$11(225)/(441), **e** $\sum$3 (112)/ $(\overline{552})$, and **f** $\sum$3(114)/(110) (Reprinted with permission from Voyiadjis and Yaghoobi 2016)

CTB, Fig. 17 shows that the first stress relaxation does not occur immediately after the first dislocation nucleation. The first large stress relaxation occurs with the first jump in dislocation density for single crystal thin films. The nature of first apparent strength drop in thin films with GB is more complicated due to the interaction of dislocations with GB. Figure 17 shows that the GB decreases the depth at which the first large stress relaxation occurs, and the bicrystal thin films have larger dislocation length at that depth compared to the single crystal samples. The GB itself can be a source of dislocation nucleation which can be activated at different stages of indentation. Figure 18 shows that the GB is the initial source of dislocation nucleation for $\sum 3\ (112)/\left(\bar{5}\bar{5}2\right)$ and $\sum 11(225)/(441)$ GBs, i.e., the initial dislocation nucleation occurs from the GB and not beneath the indenter. The nucleated dislocations are Shockley partial dislocations with the Burgers vectors of $\frac{1}{6}\left[11\bar{2}\right]$ and $\frac{1}{6}[112]$ for the GBs of $\sum 3\ (112)/\left(\bar{5}\bar{5}2\right)$ and $\sum 11(225)/(441)$, respectively. If the dislocation nucleation from GB occurs at the initial steps of dislocation nucleation and evolution, it will severely decrease the thin film strength which can be noted for $\sum 3\ (112)/\left(\bar{5}\bar{5}2\right)$ and $\sum 11(225)/(441)$ GBs in Fig. 17d, e. The size effects during nanoindentation can be described for all GBs incorporating the variation of total dislocation length and dislocation visualization during nanoindentation. The results show that the source exhaustion is the controlling mechanism of size effects for the initial stages of dislocation nucleation and evolution. Increasing the total dislocation length, however, the required dislocation length for sustaining the imposed deformation is provided and the source exhaustion mechanism becomes less dominant. Also, the dislocation interactions with each other become nonnegligible by increasing the dislocation content. Eventually, both bicrystal and their related single crystal thin films reach a similar hardness which indicates that the dislocation pileup does not enhance the hardening in the cases of studied S1 samples.

Figure 19 shows mean contact pressure versus indentation depth in the cases of S2 samples, i.e., larger samples. The initial responses of both single crystal and bicrystal thin films are similar. However, GB enhances the hardness for higher indentation depths. In order to unravel the underlying mechanisms of size effects for S2 samples, the variations of mean contact pressure and total dislocation length should be studied. Figure 20 compares the mean contact pressure and total dislocation density of the single crystal thin film with those of the bicrystal sample with CTB. The nanoindentation response can be divided to three different regions:

- *Region I*: There is no plasticity at this region. GB does not change the nanoindentation response of thin film.
- *Region II*: The plasticity is initiated beneath the indenter for both single and bicrystal thin films followed by a sharp stress relaxation. After the initial nucleation, the source exhaustion governs the size effects, and the required stress to maintain the plastic flow decreases by increasing the total dislocation length. In this region, the GB does not significantly change the total dislocation

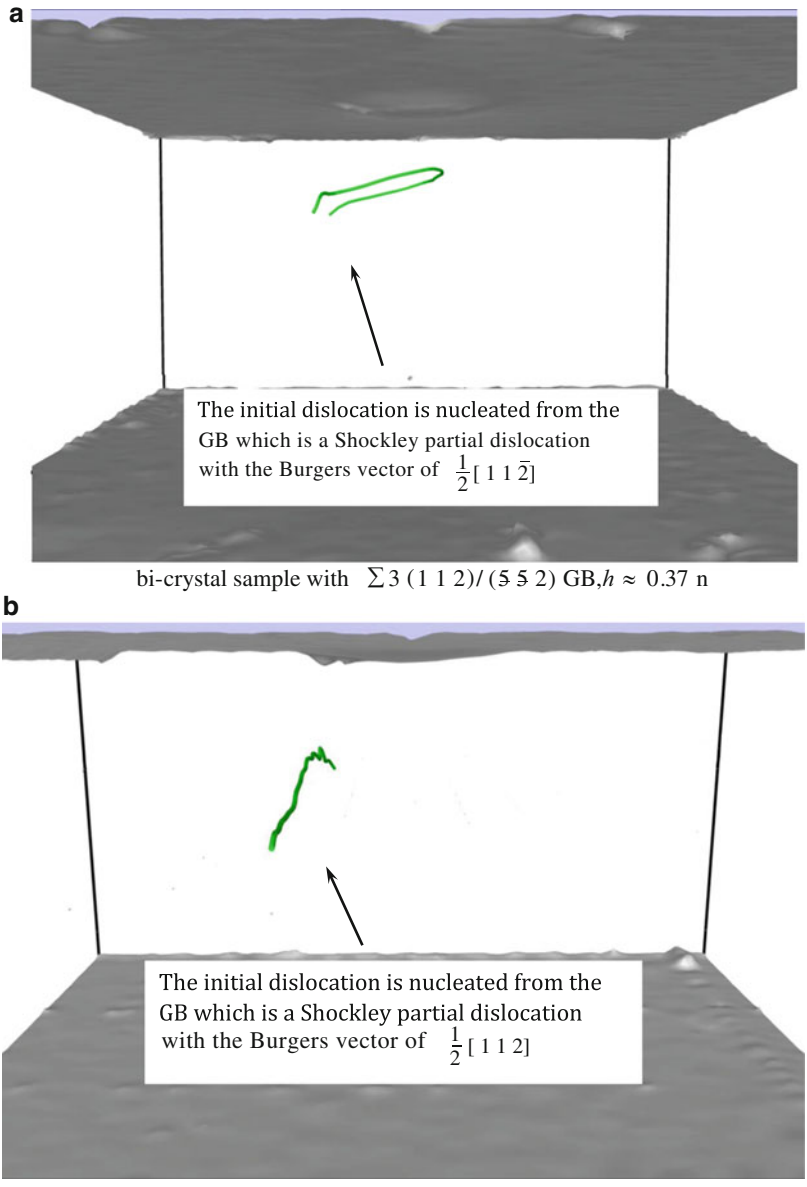

Fig. 18 Dislocation nucleation from the GB: **a** bicrystal sample with $\sum 3\ (112)/\left(\overline{5}\overline{5}2\right)$ GB, $h \approx 0.37$ nm; **b** bicrystal sample with $\sum 11(225)/(441)$ GB, $h \approx 0.43$ nm (Reprinted with permission from Voyiadjis and Yaghoobi 2016)

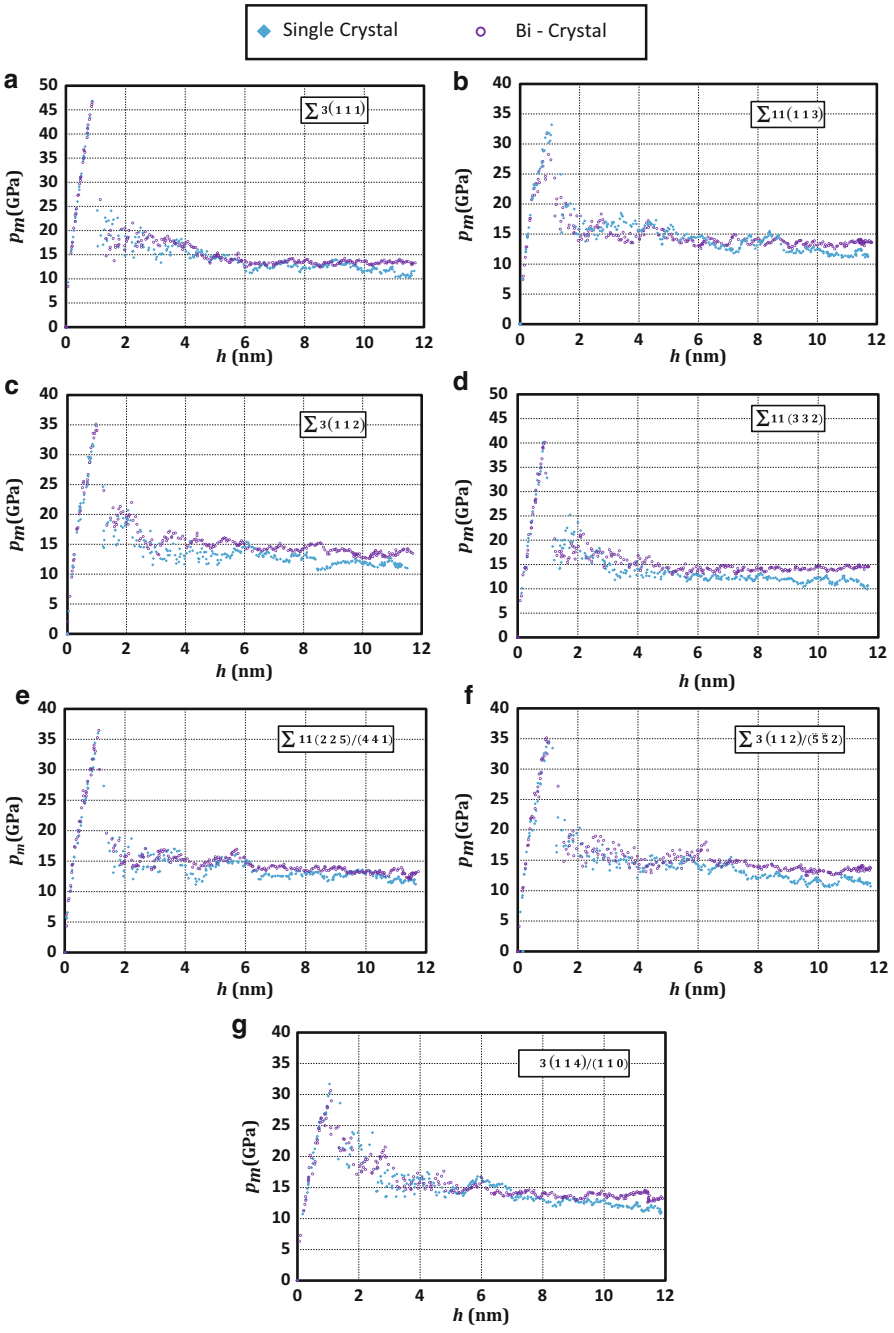

Fig. 19 Variation of mean contact pressure p_m as a function of indentation depth h for S2 single crystal and their related bicrystal samples with the grain boundaries of **a** $\sum 3(111)$, **b** $\sum 11(113)$, **c** $\sum 3(112)$, **d** $\sum 11(332)$, **e** $\sum 11(225)/(441)$, **f** $\sum 3\,(112)/\,(\bar{5}\bar{5}2)$, and **g** $\sum 3(114)/(110)$ (Reprinted with permission from Voyiadjis and Yaghoobi 2016)

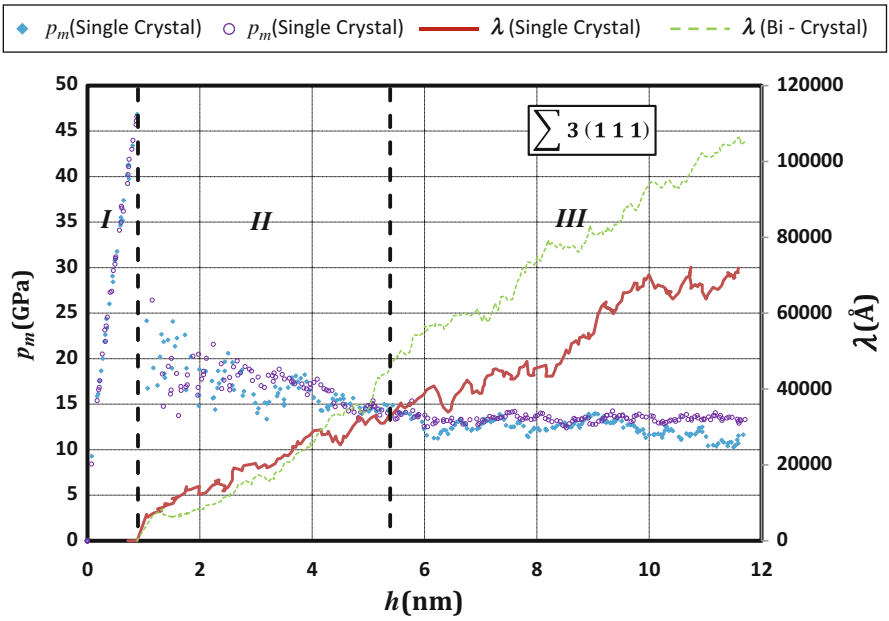

Fig. 20 Variation of mean contact pressure p_m and dislocation length λ as a function of indentation depth h for S2 bicrystal sample with $\sum 3(111)$ GB and its related single crystal sample (Reprinted with permission from Voyiadjis and Yaghoobi 2016)

length and consequently the hardness. The dominancy of source exhaustion decreases during nanoindentation as more dislocations are provided to sustain the imposed deformation. Accordingly, the hardness reduction slope decreases during nanoindentation. Eventually, the dislocations reach the GB which blocks the dislocations.

- *Region III*: Enough dislocation length is provided to sustain the imposed deformation, and the source exhaustion hardening is not active anymore. The interactions of dislocations with each other and GB become important by increasing the dislocation content. Also, the number of dislocations blocked by GB becomes considerable and the produced pile-up enhances the sample strength. Consequently, the GB enhances the nanoindentation response of thin film for S2 sample.

The dislocation visualization of the S2 thin film with and without CTB is illustrated in Fig. 21 during nanoindentation. Figure 21a, b illustrates that the initial dislocation is homogeneously nucleated beneath the indenter which is a Shockley partial dislocation with the Burgers vector of $\frac{1}{6}\left[\overline{2}11\right]$. The results show that the GB does not change the nucleation pattern. After the initial nucleation, Fig. 21c, d shows that the cross-slip is the controlling mechanism of deformation which increases the number of dislocation sources and provides the required dislocation content.

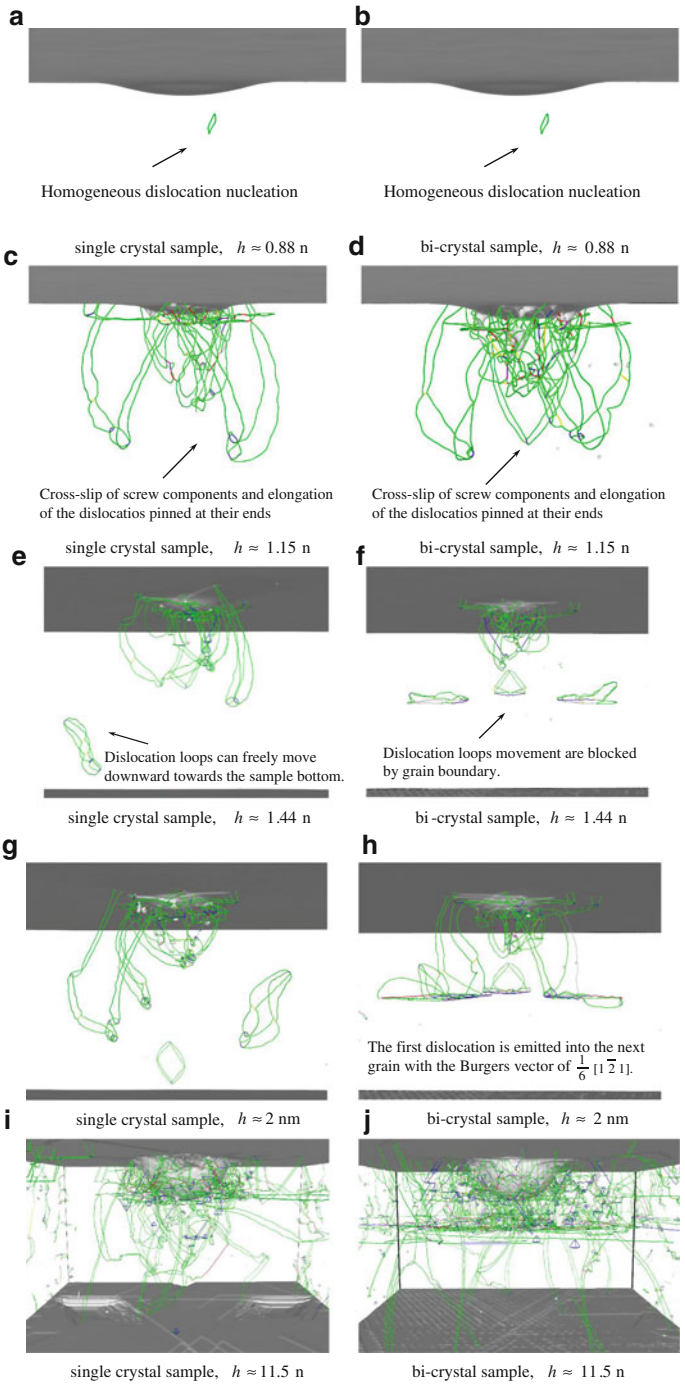

Fig. 21 (continued)

The effects of GB is still negligible on the dislocation pattern. The dislocation loops are induced by cross-slipping and pinching off of screw dislocations as the indentation depth increases. The induced loops are moving downward which are blocked by GB. Consequently, the GB starts to change the pattern of dislocation evolution. Figure 21e, f illustrates the dislocation loops movement in thin films with and without GB, respectively. The dislocation blocked by GB are eventually emitting into the next grain by increasing the indentation depth. Figure 21h illustrates the first dislocation emitting into the next grain which is a Shockley partial dislocation with the Burgers vector of $\frac{1}{6}\left[1\bar{2}1\right]$. Figure 21i, j shows the dislocation visualization of the sample at the higher indentation depths for thin film with and without GB, respectively. Although some dislocations are emitted into the next grain, the visualization results show a considerable pile-up behind the GB, while the dislocations are moving downward freely for single crystal thin film.

Figure 22 shows the variation of p_m and λ during nanoindentation for the S2 samples with different GBs and their related single crystal thin films. The observed microstructural behavior for CTB can be incorporated for all other GBs except $\sum$11(332) and $\sum$11(225)/(441) GBs. In the cases of two latter GBs, the GB enhances the hardness while the total dislocation length of thin film with GB is very close to the one without GB. The observed discrepancy is due to the fact the total dislocation length is not an appropriate factor to study the forest hardening mechanism. In the case of source exhaustion hardening, the total dislocation length dictates the amount of stress required to sustain the plastic flow. On the other hand, the density of dislocation in the plastic zone should be taken as the representative factor for the forest hardening mechanism. Voyiadjis and Yaghoobi (2016) assumed that the plastic zone is located in the upper grain. Accordingly, the total dislocation length in the upper grain λ_{upper} should be investigated during nanoindentation. The dislocations located in the upper one third is considered for single crystal thin film, and the obtained results are compared with those of bicrystal thin films. Figure 23 compares the variations of mean contact pressure and the total dislocation length located in the plastic zone during nanoindentation for thin films with and without GB. The results show that the GB increases the total dislocation length located in plastic zone and consequently enhances the hardness according to the forest hardening mechanism. The results show that the main role of GB in the cases of large thin films, i.e., S2 samples, is to modify the pattern of dislocation in a way that increases the dislocation density located in the

Fig. 21 Dislocation nucleation and evolution: **a** single crystal sample, $h \approx 0.88$ nm; **b** bicrystal sample, $h \approx 0.88$ nm; **c** single crystal sample, $h \approx 1.15$ nm; **d** bicrystal sample, $h \approx 1.15$ nm; **e** single crystal sample, $h \approx 1.44$ nm; **f** bicrystal sample, $h \approx 1.44$ nm; **g** single crystal sample, $h \approx 2.03$ nm; **h** bicrystal sample, $h \approx 2.03$ nm; **i** single crystal sample, $h \approx 11.5$ nm; **j** bicrystal sample, $h \approx 11.5$ nm (Reprinted with permission from Voyiadjis and Yaghoobi 2016)

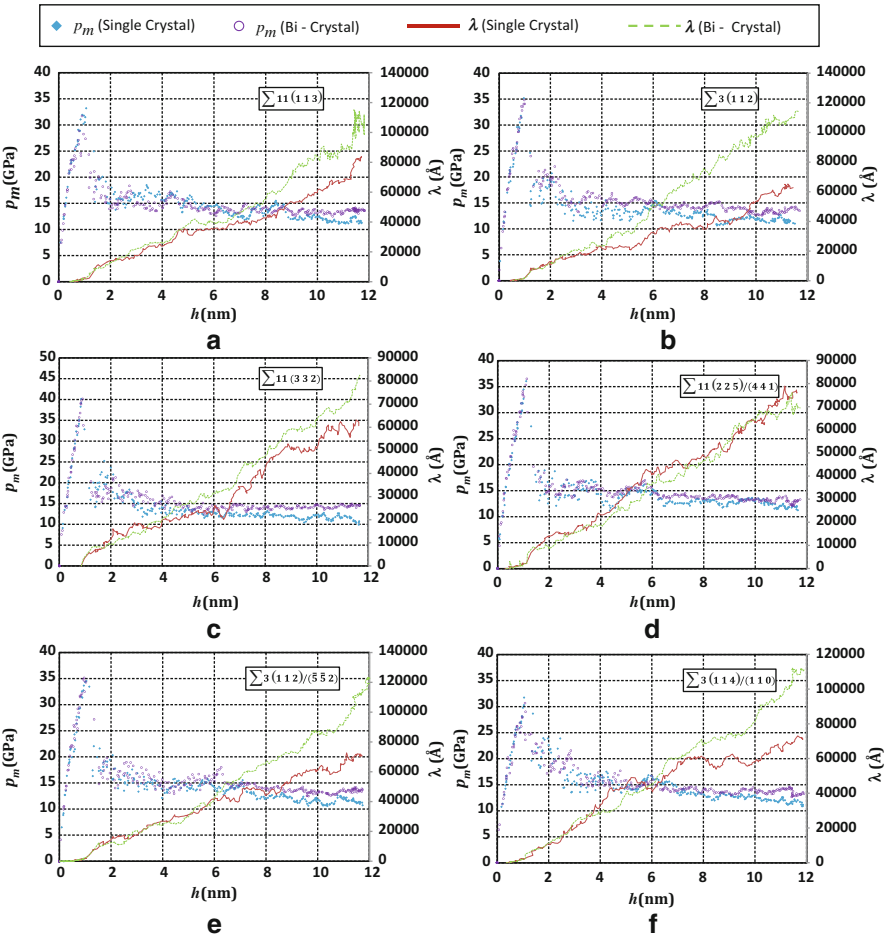

Fig. 22 Variation of mean contact pressure p_m and dislocation length λ as a function of indentation depth h for S2 bicrystal and their related single crystal samples with grain boundaries of: **a** $\sum$11(113), **b** $\sum$3(112), **c** $\sum$11(332), **d** $\sum$11(225)/(441), **e** $\sum$3 (112)/ $(\bar{5}\bar{5}2)$, and **f** $\sum$3(114)/(110) (Reprinted with permission from Voyiadjis and Yaghoobi 2016)

plastic zone and accordingly strengthen the thin films. One should note that the strain rates incorporated in the atomistic simulation are much higher than those selected for experiments. Accordingly, the interpretation of the obtained results should be carefully handled. The applied strain rate can influence both hardening mechanisms and dislocation network properties (see, e.g., Yaghoobi and Voyiadjis, 2016b; Voyiadjis and Yaghoobi, 2017; Yaghoobi and Voyiadjis, 2017). In other words, one should ensure that the observed mechanisms are not artifacts of the high strain rates used in the atomistic simulation.

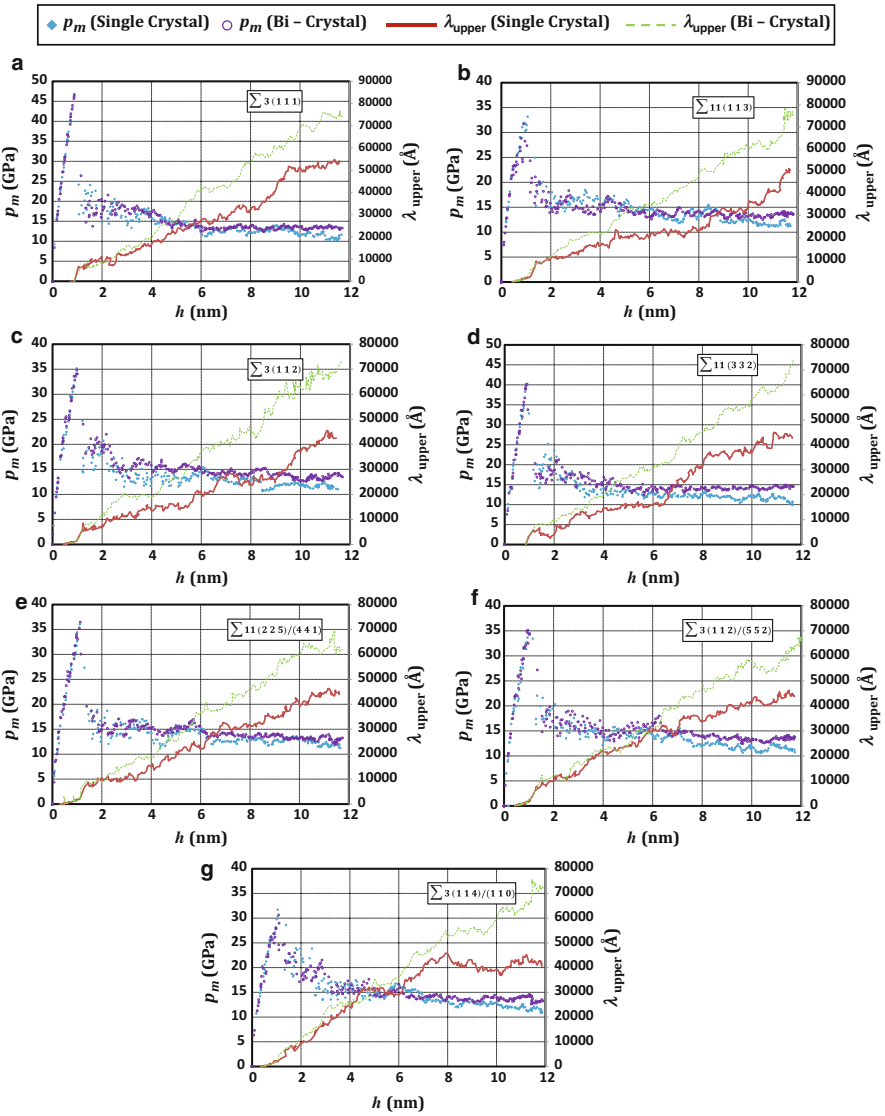

Fig. 23 Variation of mean contact pressure p_m and total dislocation length located in the upper grain λ_{upper} as a function of indentation depth h for S2 bicrystal and their related single crystal samples with grain boundaries of **a** $\sum 3(111)$, **b** $\sum 11(113)$, **c** $\sum 3(112)$, **d** $\sum 11(332)$, **e** $\sum 11(225)/(441)$, **f** $\sum 3\ (112)/\ (\overline{552})$, and **g** $\sum 3(114)/(110)$ (Reprinted with permission from Voyiadjis and Yaghoobi 2016)

References

A.H. Almasri, G.Z. Voyiadjis, Nano-indentation in FCC metals: experimental study. Acta Mech. **209**, 1–9 (2010)

R.K.A. Al-Rub, G.Z. Voyiadjis, Analytical and experimental determination of the material intrinsic length scale of strain gradient plasticity theory from micro-and nano-indentation experiments. Int. J. Plast. **20**, 1139–1182 (2004)

M.I. Baskes, Modified embedded-atom potentials for cubic materials and impurities. Phys. Rev. B **46**, 2727 (1992)

S.G. Corcoran, R.J. Colton, E.T. Lilleodden, W.W. Gerberich, Anomalous plastic deformation at surfaces: nanoindentation of gold single crystals. Phys. Rev. B **55**, 16057–16060 (1997)

C.F.O. Dahlberg, Y. Saito, M.S. Öztop, J.W. Kysar, Geometrically necessary dislocation density measurements associated with different angles of indentations. Int. J. Plast. **54**, 81–95 (2014)

M.S. Daw, M.I. Baskes, Embedded-atom method: derivation and application to impurities, surfaces, and other defects in metals. Phys. Rev. B **29**, 6443–6453 (1984)

E. Demir, D. Raabe, N. Zaafarani, S. Zaefferer, Investigation of the indentation size effect through the measurement of the geometrically necessary dislocations beneath small indents of different depths using EBSD tomography. Acta Mater. **57**, 559–569 (2009)

E. Demir, D. Raabe, F. Roters, The mechanical size effect as a mean-field breakdown phenomenon: example of microscale single crystal beam bending. Acta Mater. **58**, 1876–1886 (2010)

K. Durst, B. Backes, M. Göken, Indentation size effect in metallic materials: correcting for the size of the plastic zone. Scr. Mater. **52**, 1093–1097 (2005)

J.A. El-Awady, Unravelling the physics of size-dependent dislocation-mediated plasticity. Nat. Commun. **6**, 5926 (2015)

J.A. El-Awady, M. Wen, N.M. Ghoniem, The role of the weakest-link mechanism in controlling the plasticity of micropillars. J. Mech. Phys. Solids **57**, 32–50 (2009)

D. Faken, H. Jonsson, Systematic analysis of local atomic structure combined with 3D computer graphics. Comput. Mater. Sci. **2**, 279–286 (1994)

J.R. Greer, Nano and Cell Mechanics: Fundamentals and Frontiers. Wiley, Chichester, pp 163–190 (2013)

A. Hasnaoui, P.M. Derlet, H. Van Swygenhoven, Interaction between dislocations and grain boundaries under an indenter – a molecular dynamics simulation. Acta Mater. **52**, 2251–2258 (2004)

H. Jang, D. Farkas, Interaction of lattice dislocations with a grain boundary during nanoindentation simulation. Mater. Lett. **61**, 868–871 (2007)

C.L. Kelchner, S.J. Plimpton, J.C. Hamilton, Dislocation nucleation and defect structure during surface indentation. Phys. Rev. B **58**, 11085–11088 (1998)

C.C. Koch, I.A. Ovid'ko, S. Seal, S. Veprek, *Structural Nanocrystalline Materials: Fundamentals and Applications* (Cambridge University Press, Cambridge, 2007)

M. de Koning, R.J. Kurtz, V.V. Bulatov, C.H. Henager, R.G. Hoagland, W. Cai, M. Nomura, Modeling of dislocation–grain boundary interactions in FCC metals. J. Nucl. Mater. **323**, 281–289 (2003)

O. Kraft, P. Gruber, R. Mönig, D. Weygand, Plasticity in confined dimensions. Annu. Rev. Mater. Res. **40**, 293–317 (2010)

Y. Kulkarni, R.J. Asaroa, D. Farkas, Are nanotwinned structures in fcc metals optimal for strength, ductility and grain stability? Scr. Mater. **60**, 532–535 (2009)

J.W. Kysar, C.L. Briant, Crack tip deformation fields in ductile single crystals. Acta Mater. **50**, 2367–2380 (2002)

J.W. Kysar, Y.X. Gan, T.L. Morse, X. Chen, M.E. Jones, High strain gradient plasticity associated with wedge indentation into face-centered cubic single crystals: geometrically necessary dislocation densities. J. Mech. Phys. Solids **55**, 1554–1573 (2007)

Y. Lee, J.Y. Park, S.Y. Kim, S. Jun, Atomistic simulations of incipient plasticity under Al (111) nanoindentation. Mech. Mater. **37**, 1035–1048 (2005)

J. Li, K.J. Van Vliet, T. Zhu, S. Yip, S. Suresh, Atomistic mechanisms governing elastic limit and incipient plasticity in crystals. Nature **418**, 307–310 (2002)
S.N. Medyanik, S. Shao, Strengthening effects of coherent interfaces in nanoscale metallic bilayers. Comput. Mater. Sci. **45**, 1129–1133 (2009)
M.A. Meyers, A. Mishra, D.J. Benson, Mechanical properties of nanocrystalline materials. Prog. Mater. Sci. **51**, 427–556 (2006)
Y. Mishin, D. Farkas, M.J. Mehl, D.A. Papaconstantopoulos, Interatomic potentials for monoatomic metals from experimental data and ab initio calculations. Phys. Rev. B **59**, 3393–3407 (1999)
A.K. Nair, E. Parker, P. Gaudreau, D. Farkas, R.D. Kriz, Size effects in indentation response of thin films at the nanoscale: a molecular dynamics study. Int. J. Plast. **24**, 2016–2031 (2008)
W.D. Nix, H.J. Gao, Indentation size effects in crystalline materials: a law for strain gradient plasticity. J. Mech. Phys. Solids **46**, 411–425 (1998)
D.M. Norfleet, D.M. Dimiduk, S.J. Polasik, M.D. Uchic, M.J. Mills, Dislocation structures and their relationship to strength in deformed nickel microcrystals. Acta Mater. **56**, 2988–3001 (2008)
T.A. Parthasarathy, S.I. Rao, D.M. Dimiduk, M.D. Uchic, D.R. Trinkle, Contribution to size effect of yield strength from the stochastics of dislocation source lengths in finite samples. Scr. Mater. **56**, 313–316 (2007)
P. Peng, G. Liao, T. Shi, Z. Tang, Y. Gao, Molecular dynamic simulations of nanoindentation in aluminum thin film on silicon substrate. Appl. Surf. Sci. **256**, 6284–6290 (2010)
S. Plimpton, Fast parallel algorithms for short-range molecular dynamics. J. Comput. Phys. **117**, 1–19 (1995)
N.M. Pugno, A general shape/size-effect law for nanoindentation. Acta Mater. **55**, 1947–1953 (2007)
S.I. Rao, D.M. Dimiduk, M. Tang, T.A. Parthasarathy, M.D. Uchic, C. Woodward, Estimating the strength of single-ended dislocation sources in micron-sized single crystals. Philos. Mag. **87**, 4777–4794 (2007)
S.I. Rao, D.M. Dimiduk, T.A. Parthasarathy, M.D. Uchic, M. Tang, C. Woodward, Athermal mechanisms of size-dependent crystal flow gleaned from three-dimensional discrete dislocation simulations. Acta Mater. **56**, 3245–3259 (2008)
M.D. Sangid, T. Ezaz, H. Sehitoglu, I.M. Robertson, Energy of slip transmission and nucleation at grain boundaries. Acta Mater. **59**, 283–296 (2011)
S. Shao, S.N. Medyanik, Dislocation–interface interaction in nanoscale fcc metallic bilayers. Mech. Res. Commun. **37**, 315–319 (2010)
W.A. Soer, J.T.M. De Hosson, Detection of grain-boundary resistance to slip transfer using nanoindentation. Mater. Lett. **59**, 3192–3195 (2005)
A. Stukowski, Structure identification methods for atomistic simulations of crystalline materials. Model. Simul. Mater. Sci. Eng. **20**, 045021 (2012)
A. Stukowski, Computational analysis methods in atomistic modeling of crystals. JOM **66**, 399–407 (2014)
A. Stukowski, K. Albe, Extracting dislocations and non-dislocation crystal defects from atomistic simulation data. Model. Simul. Mater. Sci. Eng. **18**, 085001 (2010)
A. Stukowski, K. Albe, D. Farkas, Nanotwinned fcc metals: strengthening versus softening mechanisms. Phys. Rev. B **82**, 224103 (2010)
A. Stukowski, V.V. Bulatov, A. Arsenlis, Automated identification and indexing of dislocations in crystal interfaces. Model. Simul. Mater. Sci. Eng. **20**, 085007 (2012)
S. Suresh, T.G. Nieh, B.W. Choi, Nanoindentation of copper thin films on silicon substrates. Scr. Mater. **41**, 951–957 (1999)
J.G. Swadener, E.P. George, G.M. Pharr, The correlation of the indentation size effect measured with indenters of various shapes. J. Mech. Phys. Solids **50**, 681–694 (2002)
J. Tersoff, New empirical approach for the structure and energy of covalent systems. Phys. Rev. B **37**, 6991–7000 (1988)

T. Tsuru, Y. Kaji, D. Matsunaka, Y. Shibutani, Incipient plasticity of twin and stable/unstable grain boundaries during nanoindentation in copper. Phys. Rev. B **82**, 024101 (2010)
M.D. Uchic, P.A. Shade, D.M. Dimiduk, Plasticity of micrometer-scale single crystals in compression. Annu. Rev. Mater. Res. 39, 361–386 (2009)
G.Z. Voyiadjis, R.K.A. Al-Rub, Gradient plasticity theory with a variable length scale parameter. Int. J. Solids Struct. **42**, 3998–4029 (2005)
G.Z. Voyiadjis, M. Yaghoobi, Large scale atomistic simulation of size effects during nanoindentation: dislocation length and hardness. Mater. Sci. Eng. A **634**, 20–31 (2015)
G.Z. Voyiadjis, M. Yaghoobi, Role of grain boundary on the sources of size effects. Comput. Mater. Sci. **117**, 315–329 (2016)
G.Z. Voyiadjis, M. Yaghoobi, Size and strain rate effects in metallic samples of confined volumes: dislocation length distribution. Scr. Mater. **130**, 182–186 (2017)
M. Yaghoobi, G.Z. Voyiadjis, Effect of boundary conditions on the MD simulation of nanoindentation. Comput. Mater. Sci. **95**, 626–636 (2014)
M. Yaghoobi, G.Z. Voyiadjis, Atomistic simulation of size effects in single-crystalline metals of confined volumes during nanoindentation. Comput. Mater. Sci. **111**, 64–73 (2016a)
M. Yaghoobi, G.Z. Voyiadjis, Size effects in fcc crystals during the high rate compression test. Acta Mater. **121**, 190–201 (2016b)
M. Yaghoobi, G.Z. Voyiadjis, Microstructural investigation of the hardening mechanism in fcc crystals during high rate deformations. Comp. Mater. Sci. **138**, 10–15 (2017)
N. Zaafarani, D. Raabe, F. Roters, S. Zaefferer, On the origin of deformation-induced rotation patterns below nanoindents. Acta Mater. **56**, 31–42 (2008)
T.T. Zhu, A.J. Bushby, D.J. Dunstan, Materials mechanical size effects: a review. Mater. Technol. **23**, 193–209 (2008)
J.A. Zimmerman, C.L. Kelchner, P.A. Klein, J.C. Hamilton, S.M. Foiles, Surface step effects on nanoindentation. Phys. Rev. Lett. **87**, 165507 (2001)